Studies of electronic structure and thermal properties of thermoelectric materials emphasising quantitative electron diffraction

Kjetil Valset

Thesis submitted in partial fulfillment
of the requirements for the degree of
Philosophiae Doctor

Department of Physics
University of Oslo

July 2011

Series of dissertations submitted to the
Faculty of Mathematics and Natural Sciences, University of Oslo
No. 1130

ISSN 1501-7710

Cover: Inger Sandved Anfinsen.
Printed in Norway: AIT Oslo AS.

Produced in co-operation with Unipub.
The thesis is produced by Unipub merely in connection with the
thesis defence. Kindly direct all inquiries regarding the thesis to the copyright
holder or the unit which grants the doctorate.

Summary in Norwegian

Termoelektriske materialer er i stand til å gjøre om en strøm av varme mellom to varmekilder til elektrisk energi. Innen dette feltet ble det gjort mye forskning på 50 og 60 tallet. Dersom man sender strøm igjennom et termoelektrisk materiale oppnår man en motsatt effekt der man flytter varme fra en side av materialet til den andre siden. Interessen for termoelektriske materialer var derfor stor da de har mange potensielle områder for anvendelse, fra kjøleskap til produksjon av strøm fra spillvarme. Problemet var å lage termoelektriske moduler som er billige og effektive nok til å anvendes på stor skala.

Spesielt de siste 10 årene har det vært en fornyet interesse for termoelektriske materialer, en utvikling som hovedsaklig har to årsaker. Den første er bekymringer knyttet til miljøkonsekvensene av verdens økende energiforbruk. Den andre årsaken er knyttet til mulighetene som oppstår når materialene kan struktureres på atomær skala. Begrensninger som tidligere eksisterte kunne nå omgås dersom man var istand til å strukturere materialene på nye måter.

I dette arbeidet har fokuset vært på syntese og studier av billige og miljøvennlige materialer som kan benyttes i stor skala. Ved hjelp av elektronmikroskopi har vi prøvd ut nye teknikker for å studere de elektriske og termiske egenskapene til det termoelektriske materialet Mg_2Si. Slike studier er viktig for å kunne fastslå hvordan man kan optimalisere de termoelektriske egenskapene. I tillegg har vi jobbet med det termoelektriske materialet ZnSb. Ved å danne små partikler av Zn_3P_2 i ZnSb og i tillegg dope materialet med kopper fikk vi en betydelig økning i den termoelektriske effektiviteten. En videre økning av effektiviteten til ZnSb er fullt mulig og kan gjøre dette materialet sammenlignbart med de beste termoelektriske materialene som vi har i dag.

Acknowledgments

Many people have contributed to this work. Without question, the main supervisor Johan Taftø deserves my gratitude more than anyone. His scientific input and many ideas have been essential for all papers included in this thesis. The enthusiasm he shows for the work within BATE is encouraging for the other members of the group.

Co-supervisor Ole Bjørn Karlsen was also very important for most of the work. His input is central for almost all the material synthesis done in the structure physics group, yet his name seldom appears in articles. I'm also grateful to co-supervisor Anette Gunnæs for teaching me how to use the Transmission Electron Microscope, enabling me to quickly get started with the project. Terje Finstad has also become important for this work, as he has contributed through his expertise within semiconductors.

I would also like to express gratitude to my co-workers and friends in the structure physics group and BATE. Michael Böttgers previous work and input was very useful, he will be very hard to replace. I also had a lot of useful scientific discussions with Espen Flage-Larsen and Øystein Prytz. They seemingly never get tired of these discussions (not even at Christmas parties). Together with Ole Bjørn we also demonstrated that waste heat might just as well be used for beer brewing, as for generating electricity. Useful feedback was also given by Protima Rauwel on her countless visits to my office. I'm also grateful to all the other people that make this such a great place to work.

I also want to thank Yimei Zhu and Lijun Wu for their hospitality during my stay at Brookhaven Laboratories at the fall of 2010. The experience I got there proved helpful in my later work. I would also like to thank Pierre A. Stadelmann for modifying his software for me, his efforts are highly appreciated.

My family have been very supporting and I hope they by reading this thesis might get a clearer picture of what I have been working on for the last years. To quote Enrique Jardiel Poncela: "When something can be read without effort, great effort has gone into its writing". You can evaluate my effort through the following chapters.

Preface

This PhD project was carried out within The Basic and Applied ThermoElectric (BATE) initiative and supervised by Johan Taftø, Ole Bjørn Karlsen and Anette Gunnæs at the University of Oslo. Funding was given by the Norwegian Research Council under the Nanomat program.

BATE is a framework for collaboration within thermoelectricity between the University of Oslo and the University of Stavanger. The activity within BATE is focused on theory, study, synthesis and applications of thermoelectric materials.

The main focus within this project has been using quantitative electron diffraction to study charge transfer between atoms and the atomic thermal vibrations. In addition we have synthesized materials by various methods in an effort to optimize their thermoelectric properties.

The fall of 2010 I visited Brookhaven National Laboratory (BNL). This stay resulted in paper III in collaboration with Yimei Zhu and Lijun Wu at BNL.

The first paper is written on the occasion of 65th birthday of Professor John Spence. Bloch wave simulations have been essential in the electron diffraction simulations done in this thesis and in paper I the symmetries of the Bloch waves in the 17 two-dimensional space groups are classified. In addition other symmetry aspects related to electron refraction at interfaces are adressed. Paper II and III are related to convergent electron beam diffraction performed on Mg_2Si. In paper II we apply this technique to study the bonding between atoms in Mg_2Si. In paper III we use this technique to study the anharmonic vibrations of the Mg atoms. In paper IV we have synthesized the material ZnSb, and added extra zinc and phosphorus to form particles of Zn_3P_2. By additional doping with copper we achieved a significant increase in the thermoelectric figure of merit.

Contents

Chapter 1

Introduction

From 2009 to 2010 the world energy consumption grew more than 5 % and non OECD countries accounted for 84 % of growth in energy use [1]. There are great concerns associated with the emission of greenhouse gases (most notably CO_2) caused by increased consumption of fossil fuels, as non OECD countries develop an energy consumption closer to what is found in developed countries. Electricity generation from renewable sources and strategies for more efficient energy consumption are therefore areas of great importance as the world population and energy consumption keep increasing.

Thermoelectric materials are capable of converting a heat flow between two heat reservoirs into electrical energy, making them interesting for applications within power generation. Thermoelectric modules are easy to produce and reliable as they have no moving parts. They may easily be utilized on small as well as large scale and would require little maintenance [2, 3].

One problem that limits the areas of application for thermoelectric devices is the efficiency, which is typically below 10 % for the best thermoelectric materials. Due to the low efficiencies, large scale usage has sometimes been believed to be limited to vehicle exhaust heat recovery [4]. Another problem is that many of the best thermoelectric devices are dependent on toxic and expensive materials that are limited in supply, most notable tellurium. 90 % of today's tellurium comes from copper refining and the remaining reserves from this source is only 22.000 metric tons [5]. Devices made from this scarce material would have limited potential for widespread use.

If research on thermoelectric materials are to be justified on the world's need of renewable energy, the focus must be on materials with potential for large scale usage. In this Ph.D. work we therefore study materials with cheaper elements (i.e. Zn, Sb, Mg and Si). In addition, we have focused on methods for synthesizing bulk materials that may easily be scaled up on an industrial scale.

Establishing techniques for studies of thermoelectric materials by Transmission Electron Microscope is central in this work. Through these techniques, important properties of the thermoelectric materials may

be quantified, such as atomic bonding and harmonic and anharmonic atomic vibrations. The corresponding parameters are closely related to the electric and thermal properties of the material. In addition we have significantly improved the thermoelectric properties of bulk ZnSb, by doping and nanostructuring.

A focus in the Basic and Applied Thermoelectric Initiative has been on thermoelectric heat pumps. It has been shown that thermoelectric heat pumps (using the thermoelectric material Bi_2Te_3), have efficiencies comparable to commercially available heat pump´s [6]. As a thermoelectric heat pump is extremely reliable and could easily be applied on a large scale, they may be the preferred choice for such solutions. Large scale use of thermoelectric modules does not necessarily relay on making the best existing materials better, but making the efficiencies of cheap and abundant materials comparable to that of the established state of the art thermoelectric materials.

Bilbliography

[1] U.S. Energy Information Administration (EIA). Annual energy outlook 2011.

[2] F. J. DiSalvo. Thermoelectric cooling and power generation. *Science*, 285(5428):703–706, 1999.

[3] L. E. Bell. Cooling, heating, generating power, and recovering waste heat with thermoelectric systems. *Science*, 321(5895):1457–1461, 2008.

[4] C. B. Vining. An inconvenient truth about thermoelectrics. *Nat Mater*, 8(2):83–85, February 2009.

[5] U.S. Geological Survey. Mineral commodity summaries,. January 2011.

[6] J. K. Bording, V. Hansen, Ø. Prytz, and J. Taftø. Thermoelectric heat-pumps for heating of buildings. In *XIV International Forum on Thermoelectricity, Moscow*, 2011.

Chapter 2

Introduction to thermoelectricity

2.1 The thermoelectric effects

The ability of materials to directly convert a heat flow between two heat reservoirs into electrical energy was first discovered by Johann Seebeck in 1821. The discovery was based on a circuit of two dissimilar materials. If the junctions between the materials were kept at different temperatures, a voltage would arise between the ends of the circuit [1].

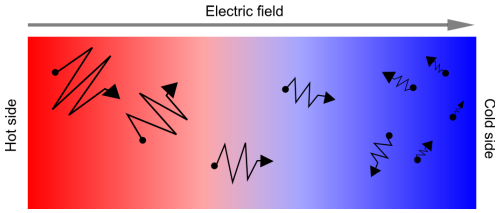

Figure 2.1: *Charge carriers (black dots) in a material diffuse faster from the hot side than carriers diffuse from the cold side. If electrons are the majority carriers, an electric field will be established from the hot side to the cold side. The voltage that sets up this electric field is called the Seebeck voltage.*

When a temperature drop is present over a sample the charge carriers at the hot end will diffuse faster to the cold end than the less energetic charge carriers at the cold end will diffuse in the opposite direction [2]. The diffusion gives rise to a flow of charge carriers from the hot side to the cold side until the force from the resulting electric field counterbalance the thermal diffusion. This was the underlying effect behind Johann Seebeck's discovery and the voltage that sets up this electric field is now called the Seebeck voltage. When two thermoelectric materials are connected together as in Seebeck's circuit, this voltage (V) can be described as V=α_{ab}(T$_{hot}$-T$_{cold}$), where α_{ab} is the difference in Seebeck coefficient for material a and b and T$_{hot}$ and T$_{cold}$ are the temperatures at the hot and cold junctions.

13 years later the watchmaker Peltier discovered that if a current was passed through such a circuit, a temperature gradient would arise between the junctions. A rate of heating, Q, would occur at one junction and a rate of cooling, -Q, at the other. These rates of cooling and heating are related to the current (I) as $\pi=\frac{Q}{I}$, where π is the Peltier coefficient. Thomson realized later that a third effect should arise, as cooling or heating as an electric current is passed through a homogeneous circuit in the presence of a temperature gradient. This is now called the Thomson effect. The Peltier coefficient and the Seebeck coefficient were then found to be related as π=Tα, where T is the temperature. The Thomson effect is usually small and is neglected in the following sections.

2.2 The Seebeck coefficient and Peltier coefficient

The Peltier coefficient can be described as the total heat current divided by the charge current [3]:

$$\pi = \frac{\sum_i h_i v_i(x)}{e\sum_i v_i(x)},$$

where h_i is the heat carried by electron i, v_i(x) is the electron speed and e is the electron charge. The thermal energy associated with one electron is equivalent to the energy difference between the electron energy (E) and the Fermi energy (E_F). By replacing the sum with an integral over energy the Peltier coefficient for metals may be described as:

$$\pi = \alpha T = \frac{\int_0^\infty (E-E_F)v(x)dE}{e\int_0^\infty v(x)dE} = \frac{\int_0^\infty \sigma(E)(E-E_F)\frac{df_0}{dE}dE}{e\int_0^\infty \sigma(E)\frac{df_0}{dE}dE}.$$

In the latter expression the electrical conductivity (σ) and the equilibrium Fermi-Dirac distribution function (f_0) is introduced. The function df_0/dE is symmetric around the Fermi level. If the conductivity σ also was symmetric or constant around the Fermi level the integral would vanish and the Seebeck/Peltier coefficient would be zero.

For a semiconductor the Seebeck coefficient can be written:

$$\alpha = \frac{1}{e}\frac{\int_0^\infty \tau(E)E^2\frac{df_0}{dE}D(E)dE}{T\int_0^\infty \tau(E)E\frac{df_0}{dE}D(E)dE} - \frac{E_f}{k_bT},$$

where D(E) is the carrier density of states, k_b is the Boltzmann constant and τ is the carrier relaxation time. Semiconductors are usually the best thermoelectric materials as σ may achieve high asymmetry around the Fermi level. Holes may also play the part as carriers in semiconductors/metals and the sign of the Seebeck coefficient will depend on which is the majority carrier. If the majority carriers are holes the Seebeck/Peltier coefficient would be positive.

2.3 Efficiency of Thermoelectric power generators

The knowledge about the general limitations imposed on a system, converting a heat flow between a warm and cold reservoir into work, was advanced in the early 19th century. The efficiency (η) of the system was defined as the power output of the system divided by the heat power supplied to the hot side of the system. It was understood that the maximum efficiency such a system could achieve was limited by the heat loss to the cold reservoir, equal to the temperature difference between the hot and the cold reservoir ($\triangle T$). The maximum efficiency any such system can achieve is called the Carnot efficiency (η_c) and is given as:

$$\eta_c = 1 - \frac{T_{cold}}{T_{hot}}. \tag{2.1}$$

The rate of heat flow through a thermoelectric material at the hot side (Q_{hot}) and cold side (Q_{cold}) may be written [4]:

$$Q_{hot} = \triangle T\kappa \cdot \frac{A}{L} + \alpha T_{hot} I - \frac{1}{2} I^2 \rho \cdot \frac{L}{A}$$
$$Q_{cold} = \triangle T\kappa \cdot \frac{A}{L} + \alpha T_{cold} I + \frac{1}{2} I^2 \rho \cdot \frac{L}{A},$$

where κ is the thermal conductivity of the sample, A and L is the area and length of the thermoelectric material, I is the current and ρ is the resistivity. The second terms in the sums can be recognized as the Peltier heat transport. The last term is the Joule heating that occurs in the thermoelectric material and is assumed to flow equally out of the hot and cold junctions.

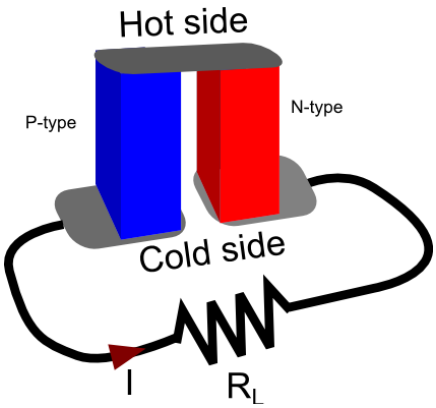

Figure 2.2: *Thermocouple configured as a power generator. R_L is the load resistance.*

A thermoelectric module is usually constructed by connecting legs of the thermoelectric materials electrically in series as in fig. 2.2. If we assume that the heat contributions from the current flowing through the legs (the Peltier term and joule heating term) are small compared to the total heat flow, the thermal

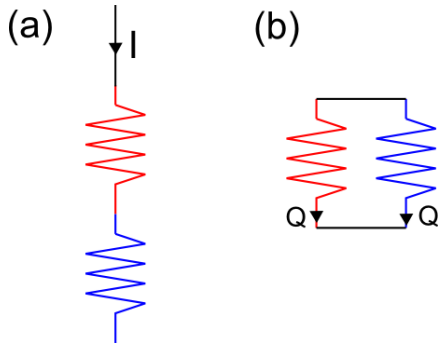

Figure 2.3: *(a) electric and (b) thermal equivalent circuits of a thermocouple. It is assumed that the joule heating and and Peltier term are small compared to the total heat flow.*

and electrical conductivity can be separated. In an electric equivalent circuit the legs will then be in series (fig. 2.3 (a)) but from a thermal point of view they will be in parallel (fig. 2.3 (b)). Holes and electrons in p/n-type materials flow in opposite directions in the electric circuit, but they are both capable of carrying heat. Modules as in (fig. 2.2) are therefore constructed by combining p-type and n-type materials as legs.

The efficiency (η) of such a couple may be written [4]:

$$\eta = \frac{\text{energy supplied to the load(R}_L\text{)}}{\text{heat energy absorbed at hot junction}} = \frac{I^2R}{\triangle T\kappa^T - \frac{1}{2}I^2R}$$

where R is the electrical series resistance of the legs and κ^T is the thermal conductance of the legs taken in parallel. The maximum efficiency can be found as:

$$\eta_{max} = \eta_c \frac{\sqrt{1+ZT^{av}} - 1}{\sqrt{1+ZT^{av}} + \frac{T_C}{T_H}} \tag{2.2}$$

where T^{av} is given as $\frac{T_{hot}+T_{cold}}{2}$. An advantage with the latter expression is that we have separated out the Carnot efficiency, η_c. This maximum efficiency can be found when $\frac{R_L}{R} = \sqrt{1+ZT^{av}}$ [1]. In the latter expressions we have also included the total dimensionless figure of merit (ZT) for a thermocouple. If the legs have similar constants (α, σ, κ) we can write the dimensionless figure of merit of each material in a thermocouple separately as [4]:

$$ZT = \frac{\alpha^2\sigma T}{\kappa_e + \kappa_l}, \tag{2.3}$$

where κ_e, κ_l is the electronic and lattice part of the thermal conductivity. A maximum power transfer to the load can be found when R=R$_L$. The efficiency under maximum power transfer (η_P) can then be written [4]:

$$\eta_P = \frac{T_{hot} - T_{cold}}{\frac{3T_{hot}}{2} + \frac{T_{cold}}{2} + \frac{4}{Z}} \tag{2.4}$$

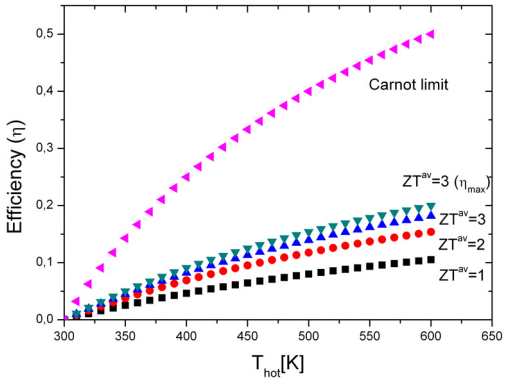

Figure 2.4: *Efficiency of a thermocouple configured as a power generator when T_{cold} is kept at 300 K, ZT^{av} is kept constant and R_L=R, where R_L is the load resistance and R is the series electrical resistance of the module . Green triangles are plotted for $\frac{R_L}{R} = \sqrt{1 + ZT^{av}}$ and represent the maximum efficiency for a given ZT (η_{max}).*

The efficiencies at maximum power transfer, η_P, at different ZT^{av} and $\triangle$T are shown in fig. 2.4 when the cold side is kept at 300 K. For ZT^{av}=3, η_{max} is also plotted and is found to be slightly higher than η_P.

2.4 Improving the figure of merit

2.4.1 Electric properties

From the expressions of η_P and η_{max} it is clear that a high ZT is needed to achieve a high efficiency. To describe the efficiency of a specific material, zT is usually used. This term describes the efficiency of a material when losses that would occur in a thermocouple module are ignored (as contact resistance etc.).

Electrons and holes both carry heat from the hot end of a semiconductor to the cold end. However, as they both carry charge with opposite sign, the thermoelectric material should have a monopolar conductivity [5]. The band gap, E_g, should be sufficiently large and an optimum bandgap can be found in the region of 10 k_bT [6]. At this value for E_g the amount of minority carriers is very small and there is nothing much to gain by increasing E_g beyond this value. Adjusting E_g by alloying has been very successful for compounds such as $Mg_2Si_xSn_{1-x}$ [7]. High valley degeneracy in the electronic bands is also benefitial, as a high effective mass may be achieved without explicitly reducing the carrier mobility [1, 8]. Low-dimensional materials have also been proposed, as quantum-confinement effects may increase the power factor ($\alpha^2\sigma$) of the material [9, 10].

The electric thermal conductivity can be written κ_e=LσT, where L is the Lorenz number. Both σ, α and κ_e

are then interdependent and by doping the carrier concentration can be changed to optimize the ratio $\frac{\alpha^2\sigma}{\kappa}$, for a given κ_l. The relation between charge carrier concentration and α, σ, κ can typically be sketched as in fig. 2.5. For an n-type semiconductor the charge carrier concentration becomes degenerate as the Fermi level is moved far into the conduction band. The asymmetry in density of states around the Fermi level may then be lost leading to a reduction in zT. An optimum doping for an n-type semiconductor is therefore normally when the Fermi level is close to the bottom of the conduction band (or close to the top of the valence band for a p-type semiconductor) [2].

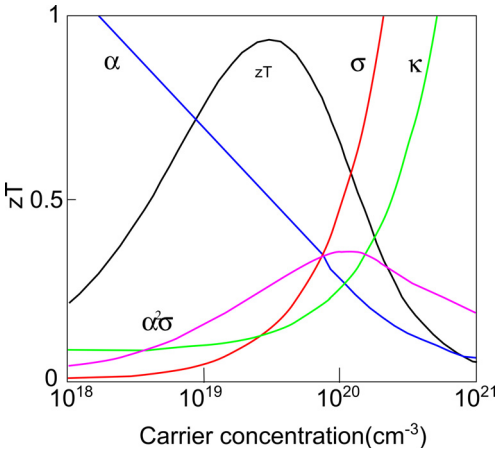

Figure 2.5: *Trends for α, σ, κ at different carrier concentrations modelled for Bi_2Te_3. Adapted from ref. [11].*

Modulation doping has been proposed as a way of increasing zT in two-phase composites [12]. One of the phases can be particles that may donate carriers to the surrounding matrix. For this effect to take place in a p-type, two-phase composite, the valence band of the particles should be lower than the valence band for the matrix ($eX^{particle}+E_G^{particle} >> eX^{matrix}+E_G^{matrix}$), as in fig. 2.6 (a). Charge carriers may then diffuse from the particles and be confined in the potential well created in the matrix (blue areas in fig. 2.6). A high carrier concentration and mobility may then be achieved simultaneously as the free carriers are separated from the donor ions. The resulting regions of excess carriers around the particles may then act as high conductivity paths for the free carriers (black arrow in fig. 2.6 (b)).

Energy filtering may also occur for carriers moving across the potential barriers between the two phases [13, 14]. Only carriers with sufficiently high energies can cross the potential barriers (green arrows in fig. 2.6 (b)), resulting in an increased Seebeck voltage.

2.4.2 Lattice thermal conductivity

The lattice thermal conductivity, κ_l, is not directly connected to κ_e, σ or α. A reduction in κ_l is desirable to increase zT and may be achieved by phonon scattering. By alloying the short wavelength phonons are scattered by point defects created by substituted atoms. The rate of scattering is determined by the mass,

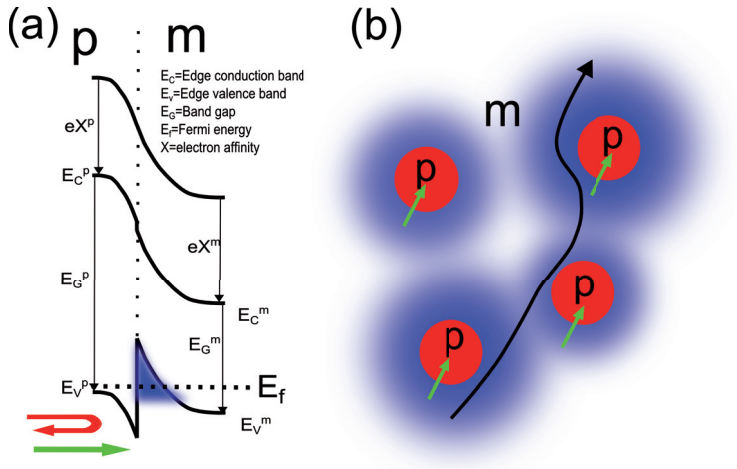

Figure 2.6: *(a)Heterojunction between material* ***p*** *and* ***m****, where the bandgap (E_g) for material* ***p*** *is larger than for material* ***m****. A potential well is created in material* ***m*** *in which charge carriers are confined (blue area). Energy filtering occurs across the potential barrier as the charge carriers with low energy are stopped (red arrow), unlike the high energy carriers (green arrow). (b) Modulation doping by particles in a matrix. Blue are the regions of excess carriers. Black arrow indicates the high conductivity path for the free carriers. Green arrows indicate energy filtering that occur across particles.*

size and interatomic force difference between the substituted and original atoms. Alloying has successfully reduced the lattice thermal conductivity in a number of materials [7, 15, 16]. The long wavelength phonons may be scattered by particles [17] and some of the reduction in κ_l in alloys may be due to precipitates in the nm region [18, 19]. By introducing both point defects and nanoparticles the thermal conductivity can be significantly reduced[20, 21]. The lower limit for κ_l achieved by atomic substitution is called the alloy limit [22]. It has recently been proposed that ordered alloys will have a thermal conductivity lower than the alloy limit due to anharmonic scattering [23]. Phonons may also be scattered by grain boundaries. Reduction of grain size to maximize the grain boundary area has successfully lowered the thermal conductivity in a number of materials [24, 25, 26].

A lower limit in κ_l can be estimated using the Einstein model for thermal conductivity, where the atoms are assumed to be harmonic oscillators with the Einstein frequency (ω_E). The atomic oscillators are coupled to each other, but the oscillations are not coherently coupled as would be the case in a crystal lattice. Based on this model an expression for the lower limit (often referred to as the amorphous limit or phonon glass limit) of the thermal conductivity ,κ_l^{min}, has been derived as [27]:

$$\kappa_l^{min} = (\frac{\pi}{6})^{1/3} k_b n^{2/3} \sum_i v_g^i \frac{T}{\theta_i} \int_0^{\frac{\theta_i}{T}} \frac{x^3 e^x}{(e^x - 1)^2} \partial x$$

where n is the number density of atoms and θ_i is the temperature corresponding to the cutoff frequency for each polarization. The phonon group velocity is assumed to be constant for all modes and the summation is over the three polarizations. θ_i is estimated from the low-frequency speed of sound and the life time of

each oscillation is assumed to be one half the period of vibration ($\tau = \pi/\omega_E$).

This approach has correctly estimated a lower limit for κ_l for a number of compounds [27]. By reducing the grain size in the thermoelectric material Bi_2Te_3, κ_l^{min} is found in agreement with this model when the average grain size is reduced to 2nm [28] and reached a value of 0.31 $\frac{W}{mK}$.

2.5 zT of some thermoelectric materials

In fig. 2.7 zT for some bulk thermoelectric materials is shown. Around room temperature zT for the best thermoelectric materials are around unity. All the materials shown are compounds with a large amount of Tellurium (except Zn_4Sb_3, Mg_2Si and $CeFe_3CoSb_{12}$) making the materials expensive to produce due to material costs.

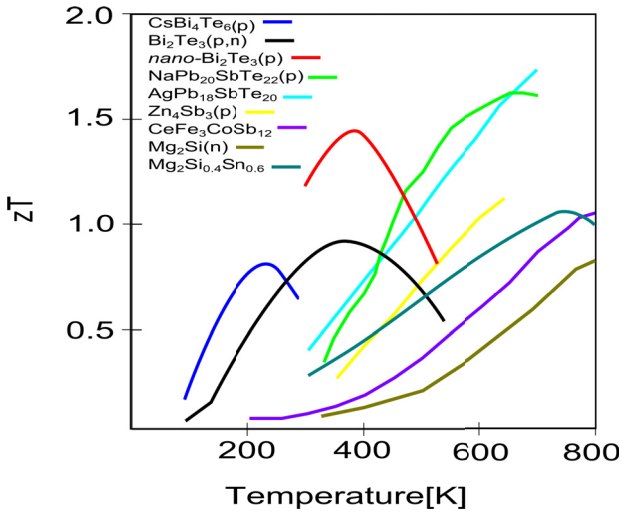

Figure 2.7: *Dimensionless figure of merit for some compounds (brackets indicate p- or n-type material). The graph is adapted from ref. [5, 29, 7]*

2.6 Thermoelectric applications

Thermoelectric materials are used in niche markets ranging from cooling of computer chips/lasers to powering interplanetary spacecrafts (as radioisotope thermoelectric generators) and silent running submarines. If thermoelectric materials are to be used for large scale cooling, they would need a ZT>3 to compete with conventional refrigerators [30]. This would be difficult to achieve, however, as thermoelectric materials become increasingly more efficient a whole range of other applications may be possible.

2.6.1 Thermoelectric heat pumps

Thermoelectric devices used as heat pumps offers several advantages over conventional heat pumps. They have no environmentally hazardous gases, no compressor or mechanical parts that could get worn, they are simple in construction and are easily scalable. The efficiency of heat pumps (usually referred to as coefficient of performance, COP) is given as the heat removed from the hot side divided by the power put into the device. For a thermocouple the COP has a maximum given as [1]:

$$COP = \frac{T^{av}(\sqrt{1+ZT^{av}}-1)}{\triangle T(\sqrt{1+ZT^{av}}+1)} + \frac{1}{2}$$

Fig. 2.8 shows the setup for a thermoelcetric heat pump and fig. 2.9 shows the COP for conventional heat pumps and heat pumps made of thermoelectric modules. It can be seen that the efficiency of thermoelectric heat pumps are comparable to conventional heat pumps.

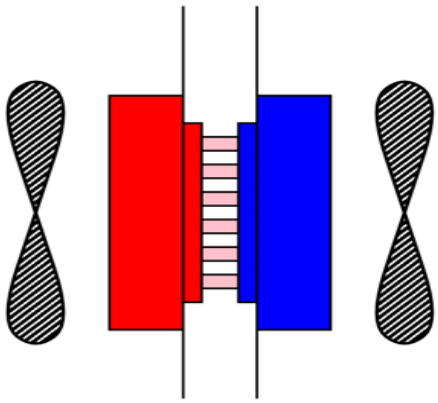

Figure 2.8: *Schematics of a thermoelectric heatpump. On each side there is a fan that directs air to/from the heat pump [31].*

2.6.2 Electrical energy from exhaust heat

For a conventional internal combustion engine only a third of the energy (at most) is available for driving the vehicle. The remaining two thirds are separated as waste heat in the exhaust stream and latent heat in the coolant system [4]. In fig. 2.10 the amount of heat energy (heat volume) is given for a 2000 cm^3 vehicle. Harvesting just a small amount of that energy would mean that less electrical energy would have to be generated by the vehicle dynamo. A goal is therefore to increase the vehicle fuel economy by 10 $\%$ through thermoelectric electricity generation [32].

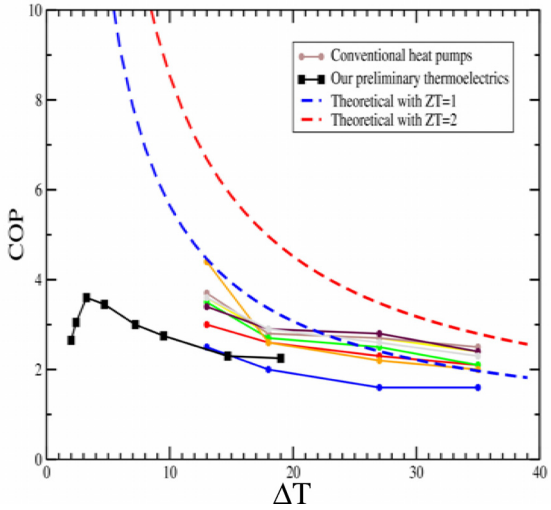

Figure 2.9: *Coefficient of performance (COP) of thermoelectric heatpumps and conventional heatpumps [31]*

2.6.3 Solar thermoelectric generators

A solar thermoelectric generator can be made as shown in fig. 2.11. An absorbent material is placed on top to absorb the sunlight. The resulting heat is transferred through the legs of a thermoelectric module. Early studies of solar thermoelectric generators where done in 1950 based on a thermocouple made of ZnSb and Bi-alloys [34]. A 50x optical concentration was then used to achieve an efficiency of about 3%. Lately more efficient generators have been made by using more efficient thermoelectric materials. When the device was tested in vacuum to prevent heat loss by convection, the peak efficiency was found at 4.6% [33]. This is below the efficiency found in solar cells, but unlike solar cells these devices don‘t have to track the sun to achieve a maximum efficiency. These devices also use only small amounts of the expensive thermoelectric materials. They are reliable and could produce electricity combined with conventional solar hot water generation.

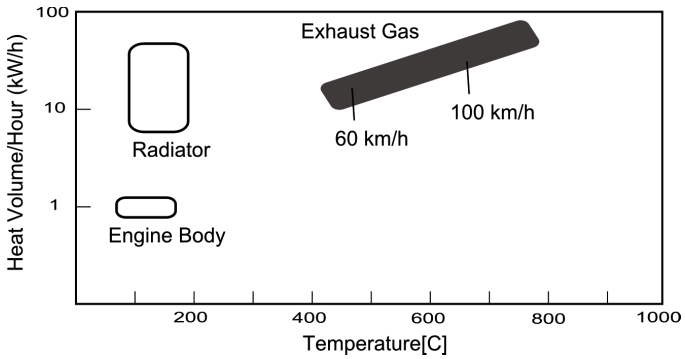

Figure 2.10: *Exhaust heat volume pr. hour vs. temperature for a 2000 cm^3 passenger car. The figure is adapted from ref. [4]*

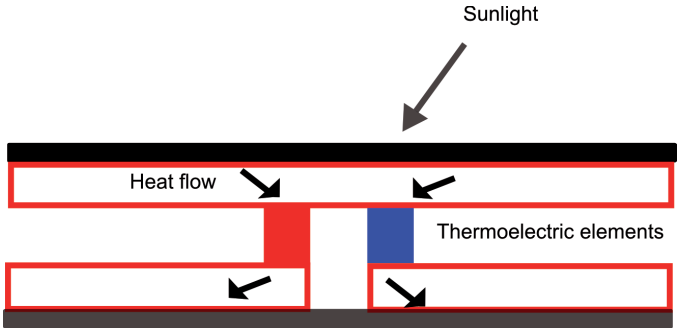

Figure 2.11: *Solar generator. On top is an absorbent material. The generated heat is directed through the thermoelectric elements. The figure is adapted from ref. [33]*

Bilbliography

[1] H. J. Goldsmid. *Applications of Thermoelectricity*. John Wiley & Sons INC, 11960.

[2] A. V. Dmitriev and I. P. Zvyagin. Current trends in the physics of thermoelectric materials. *Physics-uspekhi*, 53(8):789–803, 2010.

[3] J. S. Dugdale. The electrical properties of metals and alloys. *Edward Arnold, London*, page 103, 1977.

[4] D. M. Rowe. Thermoelectrics handbook. *Taylor and Francis*, 2006.

[5] J. R. Sootsman, D. Y. Chung, and M. G. Kanatzidis. New and Old Concepts in Thermoelectric Materials. *Angewandte chemie-International edition*, 48(46):8616–8639, 2009.

[6] G. D. Mahan. Figure of merit for thermoelectrics. *Journal of Applied Physics*, 65(4):1578–1583, 1989.

[7] V. K. Zaitsev, M. I. Fedorov, E. A. Gurieva, I. S. Eremin, P. P. Konstantinov, A. Yu. Samunin, and M. V. Vedernikov. Highly effective Mg2Si1-xSnx thermoelectrics. *Physical review B*, 74(4), JUL 2006.

[8] Y. Pei, X. Shi, A. LaLonde, H. Wang, L. Chen, and G. J. Snyder. Convergence of electronic bands for high performance bulk thermoelectrics. *NATURE*, 473(7345):66–69, May 2011.

[9] M. S. Dresselhaus, G. Chen, M. Y. Tang, R. G. Yang, H. Lee, D. Z. Wang, Z. F. Ren, J.-P. Fleurial, and P. Gogna. New directions for low-dimensional thermoelectric materials. *Advanced Materials*, 19(8):1043–1053, 2007.

[10] L. D. Hicks and M. S. Dresselhaus. Thermoelectric figure of merit of a one-dimensional conductor. *Phys. Rev. B*, 47(24):16631–16634, Jun 1993.

[11] G. J. Snyder and E. S. Toberer. Complex thermoelectric materials. *Nat Mater*, 7(2):105–114, February 2008.

[12] M. Zebarjadi, G. Joshi, G. Zhu, B. Yu, A. Minnich, Y. Lan, X. Wang, M. Dresselhaus, Z. Ren, and G. Chen. Power factor enhancement by modulation doping in bulk nanocomposites. *Nano Letters*, 11(6):2225–2230, 2011.

[13] J. Zhou, X. Li, G. Chen, and R. Yang. Semiclassical model for thermoelectric transport in nanocomposites. *Phys. Rev. B*, 82(11):115308, Sep 2010.

[14] J. M. O. Zide, D. Vashaee, Z. X. Bian, G. Zeng, J. E. Bowers, A. Shakouri, and A. C. Gossard. Demonstration of electron filtering to increase the seebeck coefficient in in0.53 ga0.47 as in0.53 ga0.28 al0.19 as superlattices. *Phys. Rev. B*, 74(20):205335, Nov 2006.

[15] P. F. P. Poudeu, J. D'Angelo, H. Kong, A. Downey, J. L. Short, R. Pcionek, T. P. Hogan, C. Uher, and M. G. Kanatzidis. Nanostructures versus solid solutions: Low lattice thermal conductivity and enhanced thermoelectric figure of merit in pb9.6sb0.2te10-xsex bulk materials. *Journal of the American Chemical Society*, 128(44):14347–14355, 2006.

[16] K. F. Hsu, S. Loo, F. Guo, W. Chen, J. S. Dyck, C. Uher, T. Hogan, E. K. Polychroniadis, and M. G. Kanatzidis. Cubic agpbmsbte2+m: Bulk thermoelectric materials with high figure of merit. *Science*, 303(5659):818–821, 2004.

[17] W. Kim and A. Majumdar. Phonon scattering cross section of polydispersed spherical nanoparticles. *Journal of applied physics*, 99(8), APR 15 2006.

[18] J. R. Sootsman, R. J. Pcionek, H. Kong, C. Uher, and M. G. Kanatzidis. Strong reduction of thermal conductivity in nanostructured pbte prepared by matrix encapsulation. *Chemistry of Materials*, 18(21):4993–4995, 2006.

[19] E. Quarez, K. Hsu, R. Pcionek, N. Frangis, E. K. Polychroniadis, and M. G. Kanatzidis. Nanostructuring, compositional fluctuations, and atomic ordering in the thermoelectric materials agpbmsbte2+m. the myth of solid solutions. *Journal of the American Chemical Society*, 127(25):9177–9190, 2005.

[20] W. Kim, J. Zide, A. Gossard, D. Klenov, S. Stemmer, A. Shakouri, and A. Majumdar. Thermal conductivity reduction and thermoelectric figure of merit increase by embedding nanoparticles in crystalline semiconductors. *Phys. Rev. Lett.*, 96(4):045901, Feb 2006.

[21] G. H. Zhu, H. Lee, Y. C. Lan, X. W. Wang, G. Joshi, D. Z. Wang, J. Yang, D. Vashaee, H. Guilbert, A. Pillitteri, M. S. Dresselhaus, G. Chen, and Z. F. Ren. Increased phonon scattering by nanograins and point defects in nanostructured silicon with a low concentration of germanium. *Phys. Rev. Lett.*, 102(19):196803, May 2009.

[22] C. Wan, Y. Wang, N. Wang, W. Norimatsu, M. Kusunoki, and K. Koumoto. Development of novel thermoelectric materials by reduction of lattice thermal conductivity. *Science and technology of advanced materials*, 11(4), AUG 2010.

[23] J. C. Duda, T. S. English, D. A. Jordan, P. M Norris, and W. A. Soffa. Reducing thermal conductivity of binary alloys below the alloy limit via chemical ordering. *Journal of Physics: Condensed Matter*, 23(20):205401, 2011.

[24] G. Joshi, H. Lee, Y. Lan, X. Wang, G. Zhu, D. Wang, R. W. Gould, D. C. Cuff, M. Y. Tang, M. S. Dresselhaus, G. Chen, and Z. Ren. Enhanced Thermoelectric Figure-of-Merit in Nanostructured p-type Silicon Germanium Bulk Alloys. *Nano Letters*, 8(12):4670–4674, DEC 2008.

[25] X. W. Wang, H. Lee, Y. C. Lan, G. H. Zhu, G. Joshi, D. Z. Wang, J. Yang, A. J. Muto, M. Y. Tang, J. Klatsky, S. Song, M. S. Dresselhaus, G. Chen, and Z. F. Ren. Enhanced thermoelectric figure of merit in nanostructured n-type silicon germanium bulk alloy. *Applied Physics Letters*, 93(19):193121, November 2008.

[26] B. Poudel, Q. Hao, Y. Ma, Y. Lan, A. Minnich, B. Yu, X. Yan, D. Wang, A. Muto, D. Vashaee, X. Chen, J. Liu, M. S. Dresselhaus, G. Chen, and Z. Ren. High-thermoelectric performance of nanostructured bismuth antimony telluride bulk alloys. *Science*, 320(5876):634–638, 2008.

[27] D. G. Cahill, S. K. Watson, and R. O. Pohl. Lower limit to the thermal conductivity of disordered crystals. *Phys. Rev. B*, 46(10):6131–6140, Sep 1992.

[28] C. Chiritescu, C. Mortensen, D. G. Cahill, D. Johnson, and P. Zschack. Lower limit to the lattice thermal conductivity of nanostructured bi2te3-based materials. *Journal of Applied Physics*, 106(7):073503 –073503–5, oct 2009.

[29] Jun ichi Tani and Hiroyasu Kido. Thermoelectric properties of bi-doped mg2si semiconductors. *Physica B: Condensed Matter*, 364(1-4):218 – 224, 2005.

[30] A. Majumdar. Thermoelectricity in semiconductor nanostructures. *Science*, 303(5659):777–778, 2004.

[31] J. K. Bording, V. Hansen, Ø. Prytz, and J. Taftø. Thermoelectric heat-pumps for heating of buildings. In *XIV International Forum on Thermoelectricity, Moscow*, 2011.

[32] J. Fairbanks. Thermoelectric application in vehicles status 2008. 2008.

[33] D. Kraemer, B. Poudel, H. Feng, J. C. Caylor, B. Yu, X. Yan, Y. Ma, X. Wang, D. Wang, A. Muto, K. McEnaney, M. Chiesa, Z. Ren, and G. Chen. High-performance flat-panel solar thermoelectric generators with high thermal concentration. *NATURE Materials*, advance online publication, May 2011.

[34] M. Telkes. Solar thermoelectric generators. *Journal of applied physics*, 25(6):765–777, 1954.

Chapter 3

Anharmonic vibrations in crystals

As the lattice thermal conductivity may be reduced independently of the electrical conductivity and Seebeck coefficient, routes for manipulating the thermal conductivity represent a relatively straight forward way of increasing zT. Anharmonic interatomic forces are important in reducing the lattice thermal conductivity at high temperatures. This chapter therefore discuss the lattice thermal conductivity with emphasis on anharmonicity and how it may be measured through electron diffraction.

3.1 Heat transport by lattice vibrations

The Taylor expansion of the potential energy (V) in the atomic displacements (u) for a crystal may be written as [1]:

$$V = \frac{1}{2}\sum_{\zeta\epsilon\xi}\sum_{\zeta'\epsilon'\xi'}(\frac{\partial^2 V}{\partial u_\xi(\zeta\epsilon)\partial u_{\xi'}(\zeta'\epsilon')})_0 u_\xi(\zeta\epsilon)u_{\xi'}(\zeta'\epsilon') + \text{anharmonic terms},$$

where the summation is done for all atoms (ϵ) in unit cells (ζ) and for all 3 degrees of freedom (ξ). As the energy is at a minimum when the atoms are at their equilibrium positions, the first derivative will be zero. In the harmonic approximation all other terms than the second derivative are ignored (the other terms are called anharmonic).

The atomic displacement for an isotropically vibrating atom can be expressed as:

$$\mathbf{u}(\epsilon\zeta,t) = \frac{1}{(n_\zeta m(\epsilon))^{1/2}}\sum_{j\mathbf{q}}\frac{E_j(\mathbf{q})^{1/2}}{\omega_j(\mathbf{q})}e^{i(\mathbf{q}\mathbf{r}(\epsilon\zeta)-\omega_j(\mathbf{q})t)},$$

where $\mathbf{q}$ is the wavevector, $\mathbf{r}(\epsilon\zeta)$ is the position of atom ϵ in unit cell ζ, m(ϵ) is the mass of atom ϵ, ω is the vibration frequency, E($\mathbf{q}$) is the vibration energy given by the Bose-Einstein relation and n_ζ is the

number of unit cells in the material. A solution of Newton's equation of motion for the atoms result in $3n_\epsilon$ solutions (n_ϵ is number of atoms in the unit cell) called branches (j) where each branch is associated with n_ζ **q** vectors. There are 3 solutions for each atom as there are 3 degrees of freedom. For a material with more than one atom in the primitve unit cell there will be three branches with a frequency converging to 0 as **q** approach zero (the acoustic branches). The remaining 3n-3 branches are the optic branches.

These quantized atomic displacements will travel through the crystal as waves (phonons) and a net flow of phonons will occur in a crystal between two areas of different phonon number, N. By solution of the Boltzman equation in the presence of a temperature gradient in the z-direction, the rate of the change of phonon number can be written as:

$$\frac{\partial N}{\partial t} = -v_g \frac{\partial N_0}{\partial T}\frac{\partial T}{\partial z}$$

where v_g is the phonon group velocity and N has been replaced by N_0. This is done assuming the phonon distribution in the presence of a temperature gradient is not too different from the phonon distribution in equilibrium (N_0). Steady state is established as there will be scattering processes that oppose the drift of phonons. In the relaxation-time method it is assumed that the phonon distribution is restored to thermal equilibrium at a rate proportional to the distribution departure from equilibrium. Then the sum of the scattering term and the drift term is zero and can be written:

$$-(\frac{\partial N(\mathbf{q},t)}{\partial t})_{drift} = (\frac{\partial N(\mathbf{q},t)}{\partial t})_{scattering} = \frac{N_0(\mathbf{q},t) - N(\mathbf{q},t)}{\tau},$$

where τ is the phonon relaxation time for the scattering process. Impurities, particles, grain boundaries etc. may contribute to the relaxation time and the contribution from each scattering process may be added by Matthiessens rule as:

$$\frac{1}{\tau_{total}} = \frac{1}{\tau_1} + \frac{1}{\tau_2} + ..$$

The heat flow (Q) in the presence of a heat gradient in the z-direction can be written as:

$$Q = \sum_q N(\mathbf{q})\hbar\omega v_g(\mathbf{q}) = -\kappa_l \frac{dT}{dz} = -9n_a k_B \frac{v_g^2}{3}(\frac{T}{\theta_D})^3 \int_0^{\frac{\theta_D}{T}} \tau(x)\frac{x^4 e^x}{(e^x-1)^2}\partial x \frac{dT}{dz},$$

where $x = \frac{\hbar\omega}{k_b T}$, n_a is the number of atoms in the solid and κ_l is the lattice thermal conductivity of the sample. In the expression for Q the Debye approximation is used under the assumption that the Brillouin zone can be approximated as a sphere and that all phonons have the same velocity. The frequency within the Brillouin zone is then proportional to ω^2 and the integration over the Brillouin zone is taken up to the Debye temperature θ_D, corresponding to the cutoff frequencys $\omega_D(=\frac{\theta_D k_b}{\hbar})$ at the edge of the Brillouin zone. In addition the optical branches are ignored as thay have a low group velocity compared to the acoustic branches. The heat capacity can be written as [2]

$$C = 9n_a k_B (\frac{T}{\theta_D})^3 \int_0^{\frac{\theta_D}{T}} \frac{x^4 e^x}{(e^x-1)^2}\partial x.$$

The lattice thermal conductivity may then be written as:

$$\kappa_l = \frac{1}{3} v_g \int_0^{\frac{\theta_D}{T}} C(x) l(x) \partial x,$$

where l(x) is the phonon mean free path defined as τ(x)v$_g$. The heat capacity C(x) includes a T^3 term which describes the change in κ_l at low temperatures.

3.2 Thermal resistance due to anharmonic interatomic forces

If the harmonic approximation were always valid the thermal conductivity of a perfect crystal would go to infinity at increasing temperatures. However, anharmonic forces will always be present as a crystal with only harmonic forces would have no thermal expansion, no temperature dependency of the elastic constants and many other properties not present in real crystals [1]. At temperatures close to θ_D, the anharmonic terms will be increasingly important. This is the case as the anharmonic terms will in effect make the phonons interchange energy with each other. The effect due to the cubic term in the interatomic potential can be expressed as a process where two phonons interact and create a third phonon as in fig. 3.1 (this process can also be reversed). The relations that have to be fulfilled for such a process to occur are:

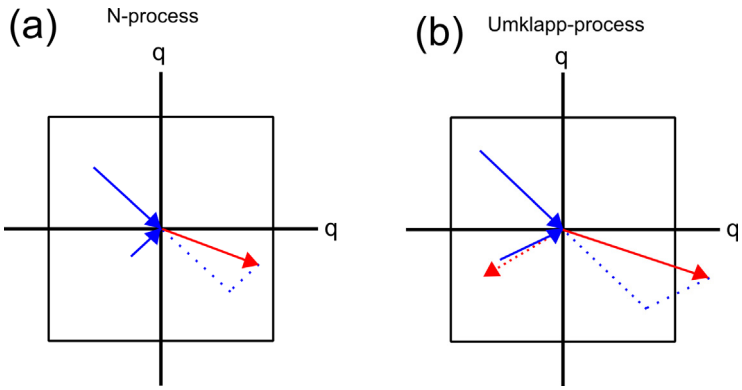

Figure 3.1: *(a) N-process where two phonons combine to produce a third phonon with wave vector inside the Brillouin zone. (b) U-process where two phonons combine to produce a phonon with wave vector outside the Brillouin zone, creating a resistive process [2].*

$$\omega_1 + \omega_2 = \omega_3 \tag{3.1}$$

$$\mathbf{q}_1 + \mathbf{q}_2 = \mathbf{q}_3 + \mathbf{g}, \tag{3.2}$$

where **g** is a reciprocal lattice vector. When **g** is zero the interaction is called an N-process. The effect of the N process could be taken into account by shifting the Bose-Einstein distribution of the phonons. The

N-process does not lower the thermal resistivity directly, but could have an indirect influence when other scattering processes are involved by redistributing the phonon distribution. However, if there are other strong scattering mechanisms involved, the N-process can often be ignored. When $\mathbf{g} \neq 0$ the process is called Umklapp. The Umklapp process is a source of thermal resistance as two phonons combine creating a third phonon, where at leat one phonon has a wave vector reaching outside the Brillouin zone. In this process there will be a sign reversal for at least one wave vector, leading to a reduction in the net heat flow. In perfect or almost perfect non-metallic crystals at temperatures above θ_D, the Umklapp process caused by anharmonic thermal vibrations will usually be the main source of thermal resistance.

3.3 Temperature trends in the lattice thermal conductivity

Figure 3.2 shows a sketch of a typical lattice thermal conductivity of a crystal with little defects. At very low temperatures the lattice thermal conductivity will be determined by boundary scattering as the lattice conductivity is dominated by long wavelength phonons. At higher temperatures the conductivity reflects the T^3 relation of the heat capacity (blue curve). A maximum in thermal conductivity is often reached at temperatures T=θ_D/20 [3]. The value of κ_l at this maximum is typically limited by lattice impurities and defects. At these temperatures the Umklapp process will be more frequent and results in an exponential drop in κ_l (red curve). At even higher temperatures the lattice heat capacity will be a constant. The thermal conductivity is then $\propto T^{-1}$ due to the Umklapp process [4].

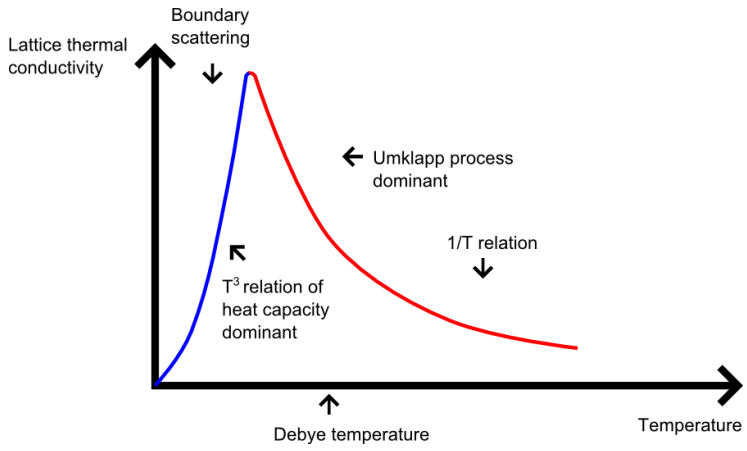

Figure 3.2: *Typical trend in lattice thermal conductivity at increasing temperatures. At low temperatures the conductivity is limited by boundary scattering. At high temperatures it is limited by Umklapp-scattering.*

3.4 Diffraction from crystals with harmonic and anharmonic interatomic forces

3.4.1 The B-factor

In the kinematical approximation for electron scattering the intensity when absorption is ignored, can be written [1]:

$$I(\mathbf{s}) \propto \sum_{\zeta'\epsilon'} \sum_{\zeta\epsilon} f^e_{\epsilon'}(\mathbf{s}) f^e_{\epsilon}(\mathbf{s}) e^{2\pi i \mathbf{s}(\mathbf{r}(\zeta'\epsilon') - \mathbf{r}(\zeta\epsilon))} < e^{2\pi i \mathbf{s}(\mathbf{u}(\zeta'\epsilon') - \mathbf{u}(\zeta\epsilon))} >,$$

where $f^e_\epsilon(\mathbf{s})$ and $\mathbf{r}(\epsilon)$ are the electron scattering factor and position for atom ϵ and $\mathbf{s}$ is the scattering vector defined as $\mathbf{s} = \frac{\sqrt{(h^2+k^2+l^2}}{a}$ for a cubic crystal, where h, k, l are the Miller indices and a is the lattice parameter. The summation is done over all the atoms in all unit cells,ζ, and the bracket <> around the last term is the time average. When the harmonic approximation is used and by neglecting higher order terms in a Taylor expansion, it can be written:

$$I \propto \sum_{\zeta'\epsilon'} \sum_{\zeta\epsilon} f^e_{\epsilon'}(\mathbf{s}) e^{-W_{\epsilon'}(\mathbf{s})} f^e_{\epsilon}(\mathbf{s}) e^{-W_{\epsilon}(\mathbf{s})} e^{2\pi i \mathbf{s}(\mathbf{r}(\zeta'\epsilon') - \mathbf{r}(\zeta\epsilon))},$$

where $W_\epsilon(s)$ is called the Debye-Waller factor for atom ϵ. For isotropic vibrating atoms the Debye-Waller factor is written:

$$W_k = 8\pi^2 < u(\epsilon)^2 > s^2 = Bs^2,$$

where $< u(\epsilon)^2 >$ is the mean square displacement for atom ϵ and B is called the (isotropic) B-factor. If we use the Debye approximation for the phonon density of states, the mean square displacement can be expressed as:

$$< u(\epsilon)^2 >= 3\hbar(\frac{\hbar}{k_b\theta_D})^3 \int_0^{\omega_D} E(\omega)\omega d\omega = \frac{3\hbar^2 T}{m k_B \theta_D^2}[\varphi(\frac{\theta_D}{T}) + \frac{1}{4}\frac{\theta_D}{T}]$$

The last term in the latter expression is valid for a monoatomic crystal and $\varphi(\frac{\theta_D}{T})$ is the Debye integral function defined as:

$$\varphi(x) = \frac{1}{x}\int_0^x \frac{y}{e^y - 1} dy.$$

At temperatures higher than θ_D the mean square displacement approaches:

$$< u^2 >= \frac{3\hbar^2 T}{m k_B \theta_D^2}$$

and at low temperatures it is a constant given as:

$$< u^2 >= \frac{3\hbar^2}{4 m k_B \theta_D}.$$

If the harmonic approximation is valid, the Debye temperature can be found from the linear slope in $< u^2 >$ vs. temperature. The anharmonic interatomic forces become more important at temperatures above θ_D. This leads to a larger increase in $< u^2 >$, and the deviation from a linear slope in $< u^2 >$ at increasing

temperatures is an indication of the anharmonic contribution to the atomic vibrations.

3.4.2 Anharmonic vibrations in fluorite structures

Cubic fluorite structures (XY_2) can be described as an arrangement with atom X in a face centered arrangement and atom Y at tetrahedral positions (fig. 3.3). The arrangement at the tetrahedral position can be sketched as in fig. 3.4 (a) where atom Y is surrounded by four atoms of type X and four vacant positions. It has been found that some reflections with different h,k,l indices deviates in intensity even if the scattering vectors have the same lenght [5, 6, 7]. This could not be explained by harmonic theory and two different models have been developed to describe these deviations. Willis explained the systematic deviation in in-

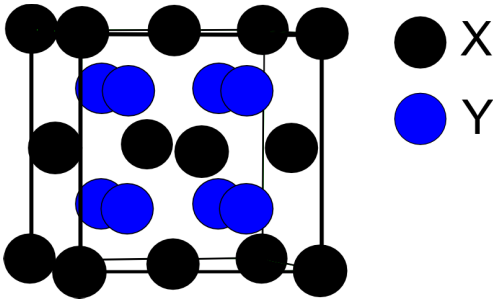

Figure 3.3: *Fluorite structure where X are cations at a face centered arrangement and Y are anions at tetrahedral positions.*

tensity as a shift in the position (δ) of atom Y along the $< 111 >$ directions of the crystal. This shift could be understood as atom Y tends to vibrate towards the vacancy sites of the tetrahedral. Four equivalent positions for atom Y are set around the centre of the tetrahedral, with each atom vibrating harmonically. By this model the structure factor F could be written as:

$$F = 4b_X exp(-B_X s^2) + 8b_Y cos(2\pi hu)cos(2\pi ku)cos(2\pi ku)exp(-B_Y s^2)$$

where b_X, b_Y and B_X, B_Y are the scattering factors and B factors of atom X and atom Y, while u is the position of atom Y (u=0.25+δ).

Another model was proposed where the atomic vibrational displacement for atom Y was expanded towards the vacancy sites. Atom Y is now at the centre at the tetrahedron with anisotropic vibration described by the anharmonic parameter β. The resulting odde reflections can be described as:

$$F(4n \pm 1) = 4f_X^e exp(-B_X s^2)$$
$$\pm 8f_Y^e exp(-B_Y s^2)(\frac{B_Y}{4\pi a})^3 \frac{hkl}{k_B T}\beta$$

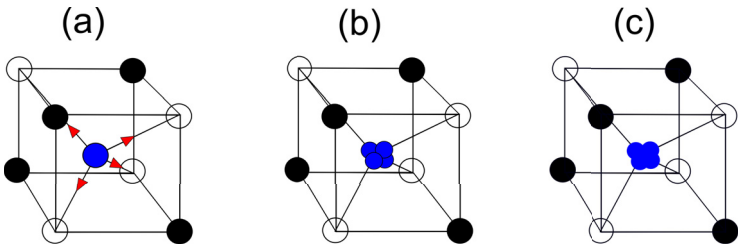

Figure 3.4: *(a) Atoms at tetrahedral positions (blue) surrounded by 4 atoms and 4 vacant sites. (b) Willis model for vibrations towards vacant sites. (c) Dawson model for anharmonic vibrations. Adapted from ref. [8]*

Both these models are able to describe the intensities of fluorite structures and they both contain three parameters that have to be found (two B factors in addition to β or δ).

Bilbliography

[1] B. T. M. Willis and A. W. Pryor. Thermal vibrations in crystallography. *Cambridge University Press*, 1975.

[2] C. Kittel. *Introduction to Solid State Physics*. John Wiley & Sons, Inc, 1976.

[3] H. J. Goldsmid. *Applications of Thermoelectricity*. John Wiley & Sons INC, 11960.

[4] R. Berman. Thermal conduction in solids. *Clarendon Press. Oxford*, -:–, 1976.

[5] B. Dawson, A. C. Hurley, and V. W. Maslen. Anharmonic vibration in fluorite structures. *Proceedings of the Royal Society of London. Series A, Mathematical and Physical Sciences*, 298(1454):pp. 289–306, 1967.

[6] M. J. Cooper, K. D. Rouse, and B. T. M. Willis. Neutron diffraction studies of anharmonic temperature factors in BaF_2. *Acta Crystallographica Section A*, 24(5):484–493, Sep 1968.

[7] B. T. M. Willis and R. G. Hazell. Re-analysis of single-crystal neutron-diffraction data on UO_2 using third cumulants. *Acta Crystallographica Section A*, 36(4):582–584, Jul 1980.

[8] K. D. Rouse, B. T. M. Willis, and A. W. Pryor. Anharmonic contributions to debye-waller factors of uo2. *Acta Crystallographica Section B-structural Crystallography and Crystal Chemistry*, B 24:117–&, 1968.

Chapter 4

Electron diffraction, Bloch waves and their symmetry

The Transmission Electron Microscope (TEM) was the main tool used in this thesis for property and structure studies of thermoelectric materials. In this chapter a brief introduction to the many beam dynamical theory of electron diffraction is given. The high energy electron interactions with the crystal, can be described by the Bloch wave formalism. This Bloch wave formalism was used when the electron diffraction experiments were simulated in paper I-III. The experimental techniques described here are convergent beam techniques which are used for accurate measurement of the electron structure factors.

4.1 Bloch waves and their symmetry

4.1.1 Bloch wave formalism

The fundamental equation in dynamical electron diffraction may be written [1]:

$$2K(S_g - \gamma^j)C_g^j = \sum_{h \neq g} U_{g-h} C_h^j$$

where K is the fast electron wave number within the crystal, C_g^j is the Bloch wave coefficients for reflection **g** and S_g and γ^j are the excitation error and anpassung associated with reflection **g**. The matrix $\sum U_{g-h}C_h + 2KS_g$ is referred to as the dispersion matrix and K >> S_g,γ^j. U_g is the Fourier potential of reflection **g** at position **r** and in the isotropic case, neglecting absorption it can be written as:

$$U_g = \frac{m}{\pi V m_0} \sum_{\epsilon} f_{\epsilon}^e(\mathbf{s}) e^{2\pi i(\mathbf{g}\cdot\mathbf{r}(\epsilon))} e^{-B_\epsilon s^2} = \frac{m^* F^e}{m_0 V \pi}$$

where f_ϵ^e and B_ϵ is the electron scattering factor and isotropic B-factor for atom ϵ, V is the unit cell volume, F^e is the electron structure factor, **s** is the scattering vector and the summation is over all the atoms in the unit cell. By defining $\mathbf{k}^j$=$\mathbf{k}_g$ + S_g + γ^j where k_g is the wave number for reflection **g**. The Bloch wave j is defined as:

$$B^j(\mathbf{r}) = \sum_g C_g^j e^{2\pi i(\mathbf{k^j}+\mathbf{g})\mathbf{r}}$$

The term $|B^j(\mathbf{r})|^2$ adopt the periodicity of the crystal and describes the high energy electron density in the crystal. The total wave function of the scattered electrons ($\psi(\mathbf{r})$) may be written as the sum of all the normalized Bloch waves:

$$\psi(\mathbf{r}) = \sum_{j=1}^{N} C_0^j B^j(\mathbf{r}) = \sum_g \phi_g(\mathbf{r}) e^{2\pi i(\mathbf{K}+\mathbf{g})\mathbf{r}},$$

where ϕ_g is the amplitude of the scattered beam g. In a Bloch wave simulation the fundamental equation is solved for a finite number of beams to find the Bloch wave eigenvectors and anpassungen associated with each beam. As the scattering angles are small the amplitude will only vary with thickness z. The intensity (I_g) of a scattered beam g may now be found from the square of the scattered amplitude and including absorption (μ) it can be written as:

$$I_g(z) = \sum_{j,j'} C_0^j C_g^j C_0^{j'*} C_g^{j'*} e^{2\pi i(\gamma^j - \gamma^{j'})z} e^{-(\mu^j + \mu^{j'})z}.$$

4.1.2 Bloch wave symmetry

By utilizing the symmetry of the dispersion matrix, the Bloch wave simulations may be simplified [2, 3, 4]. By considering Bloch wave symmetries, additional insight might be gained into aspects of the electron beam interaction with the crystal, such as anomalous absorption. The symmetries can be found from the following relations:

$$\begin{aligned} 2K\gamma^j(\mathbf{s}+\mathbf{h}) &= 2K\gamma^j(\mathbf{s}) + 2KS_h \\ C_g^j(\mathbf{s}+\mathbf{h}) &= C_{g-h}^j(\mathbf{s}) \\ \mu^j(\mathbf{s}+\mathbf{h}) &= \mu^j(\mathbf{s}) \end{aligned}$$

In crystals with inversion symmetry the dispersion matrix will be hermitian so then we also have:

$$2K\gamma^j(\mathbf{s}) = 2K\gamma^j(-\mathbf{s})$$

From the symmetry of the dispersion matrix, an asymmetrical unit may be defined as the smallest number of reciprocal vectors in which the whole set of vectors may be constructed by application of symmetry operators. In fig. 4.2, the asymmetric sectors for the 17 two-dimensional space groups are presented. Each vector in an asymmetrical unit will have a corresponding vector in the other asymmetrical units with

the same excitation error. By application of symmetry operators the whole set of reciprocal vectors may then be constructed. In fig. 4.3 representations of the Bloch wave symmetries for the 17 two-dimensional space groups are presented. In the following section an example is given to illustrate how symmetry considerations may simplyfy Bloch wave calculations.

4.1.3 Symmetry Example

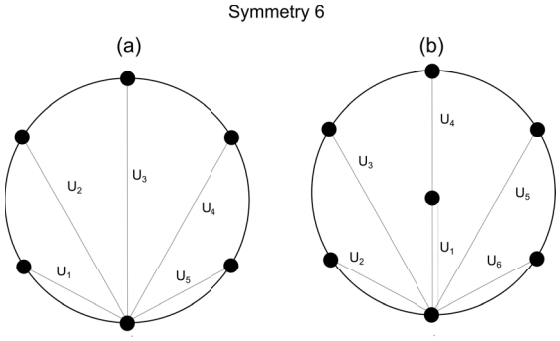

Figure 4.1: *(a) Fourier potentials with 6 fold symmetry. (b) Fourier potentials with 6 fold symmetry with the incident beam in the middle. Large circles indicate the Ewald sphere.*

Fig. 4.1 (a) shows the diffraction symmetry 6, where all Fourier potentials have no excitation error. From the figure it can be seen that U_1=U_5 and U_2=U_4. The resulting dispersion matrix can be written as:

$$\begin{bmatrix} -2K\gamma & U_1 & U_2 & U_3 & U_2 & U_1 \\ U_1 & -2K\gamma & U_1 & U_2 & U_3 & U_2 \\ U_2 & U_1 & -2K\gamma & U_1 & U_2 & U_3 \\ U_3 & U_2 & U_1 & -2K\gamma & U_1 & U_2 \\ U_2 & U_3 & U_2 & U_1 & -2K\gamma & U_1 \\ U_1 & U_2 & U_3 & U_2 & U_1 & -2K\gamma \end{bmatrix} \begin{bmatrix} C_0 \\ C_1 \\ C_2 \\ C_3 \\ C_4 \\ C_5 \end{bmatrix} = 0$$

The eigenvectors can be read from the symmetry 6 in fig. 4.3 and will then have the form:

$$\begin{bmatrix} 1 \\ e^{i\phi} \\ e^{i2\phi} \\ e^{i3\phi} \\ e^{i4\phi} \\ e^{i5\phi} \end{bmatrix},$$

where ϕ is a phase factor given for the different anpassungen in fig. 4.3 (6 (ϕ=0), 6′ (ϕ=π), $\frac{2\pi}{6}$, $-\frac{2\pi}{6}$, $\frac{4\pi}{6}$,

$-\frac{4\pi}{6}$. By using this vector on any of the rows in the dispersion matrix, the anpassungen are found as:

$$\begin{aligned}\gamma^{6} &= 2U_1 + 2U_2 + U_3 \\ \gamma^{6'} &= -2U_1 + 2U_2 - U_3 \\ \gamma^{\frac{2\pi i}{6}} &= \gamma^{\frac{-2\pi i}{6}} = U_1 - U_2 - U_3 \\ \gamma^{\frac{4\pi i}{6}} &= \gamma^{-\frac{4\pi i}{6}} = -U_1 - U_2 + U_3\end{aligned}$$

Hence, instead of solving a 6x6 matrix to find the anpassungen, the solutions can be found directly from the symmetry of the dispersion matrix. If there had been two reflections in each assymetric sector the solutions could be found by solving a 2x2 matrix.

In fig. 4.1 (b) the situation is shown where the central beam is in the middle surrounded be 6 reflections in a 6 fold symmetry. For simplicity it is assumed that the central beam has excitation error S, and the remaining six beams are on the Ewald sphere. From the figure it is seen that U_1=U_2=U_6 and U_3=U_5. Solutions can now be found by solving:

$$\begin{bmatrix} -2K\gamma - 2KS & U_1 & U_1 & U_1 & U_1 & U_1 & U_1 \\ U_1 & -2K\gamma & U_1 & U_3 & U_4 & U_3 & U_1 \\ U_1 & U_1 & -2K\gamma & U_1 & U_3 & U_4 & U_3 \\ U_1 & U_3 & U_1 & -2K\gamma & U_1 & U_3 & U_4 \\ U_1 & U_4 & U_3 & U_1 & -2K\gamma & U_1 & U_3 \\ U_1 & U_3 & U_4 & U_3 & U_1 & -2K\gamma & U_1 \\ U_1 & U_1 & U_3 & U_4 & U_3 & U_1 & -2K\gamma \end{bmatrix} \begin{bmatrix} C_0 \\ C_1 \\ C_2 \\ C_3 \\ C_4 \\ C_5 \\ C_6 \end{bmatrix} = 0$$

One of the asymmetric sectors will now also contain the central beam. This can be solved by creating a new vector:

$$\begin{bmatrix} 0 \\ 1 \\ e^{i\phi} \\ e^{i2\phi} \\ e^{i3\phi} \\ e^{i4\phi} \\ e^{i5\phi} \end{bmatrix}$$

The eigenvectors can again be found from the symmetry 6 in fig. 4.3. By using the latter vector, solutions can be found for 6′, $\frac{2\pi}{6}$, $-\frac{2\pi}{6}$, $\frac{4\pi}{6}$ and $-\frac{4\pi}{6}$ (if the vector is used on the first row the answear would always be zero). It is seen that these anpassungen are the same as found in (a). The remaining anpassungen can then be found by solving the matrix:

$$\begin{bmatrix} -2K\gamma - 2KS & 6U_1 \\ U_1 & -2K\gamma + 2U_1 + 2U_3 + U_4 \end{bmatrix} \begin{bmatrix} C_x \\ C_y \end{bmatrix} = 0$$

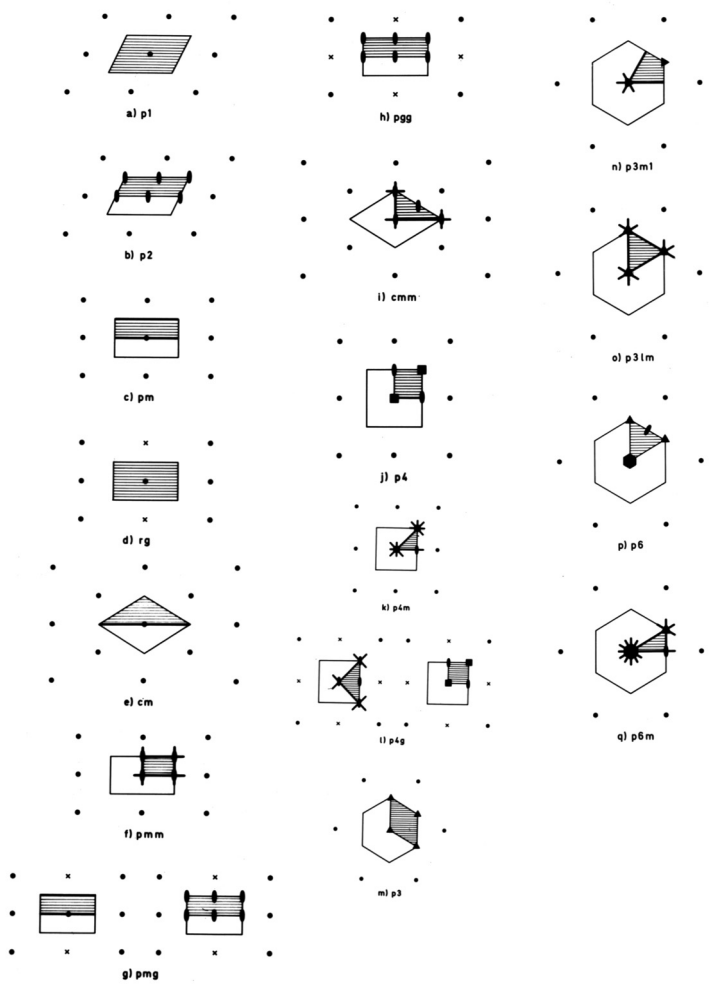

Figure 4.2: *asymmetric sectors for the 17 two dimensional space groups*

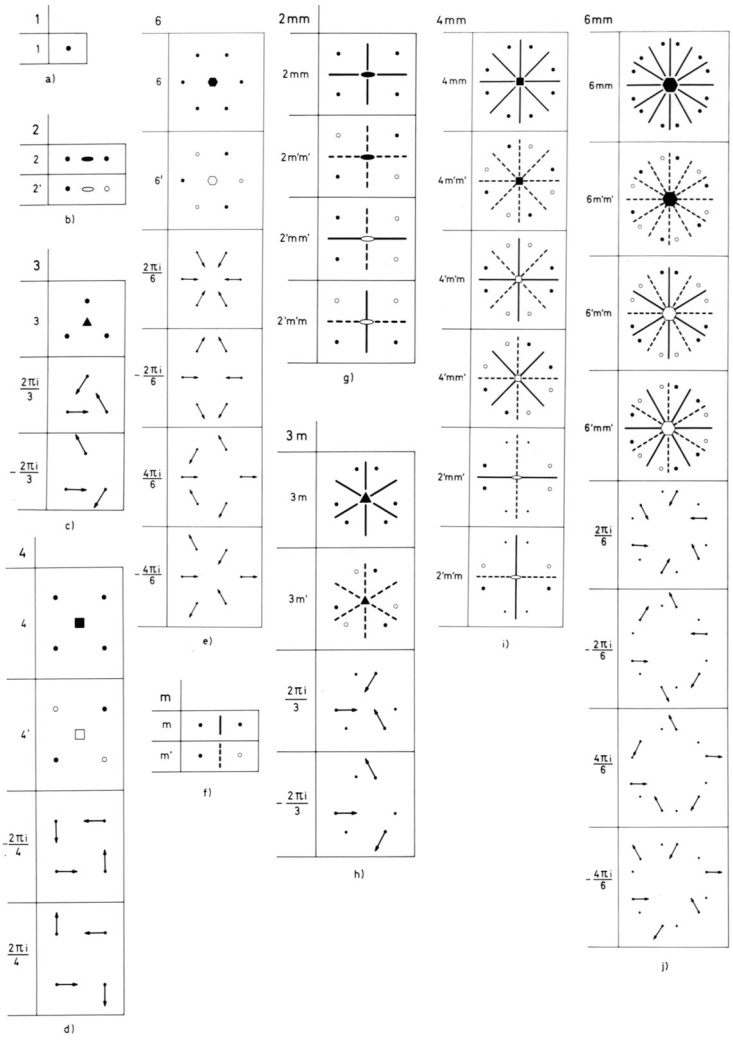

Figure 4.3: *Bloch wave symmetries for the 17 two dimensional space groups*

4.2 Convergent Beam Electron Diffraction

A procrystal is a hypothetical crystal with scattering factors of isolated atoms. The resulting structure factor will only be an approximation, as bonding between atoms in crystals will redistribute the valence electrons. This means that if the structure factor could be measured with great accuracy, the nature of the bonding (that is the electron density) could be determined quantitatively. The electron density may be found as the Fourier transform of the X-ray scattering factor f^x. An X-ray scattering factor can converted to the electron scattering factor (f^e) by using the Mott formula:

$$f^e = c\frac{Z - f^x}{s^2},$$

where c is a constant and Z is the atomic number of the atom. From the Mott formula it is evident that at small scattering vectors, **s**, a small change in f^x may lead to a great change in f^e. This situation is illustrated in fig. 4.4, where the different scattering factors for silicon is shown for a neutral atom and an atom where all the four valence electrons are removed. It is seen that at large scattering vectors the electron scattering factor f^e is not different, but there is a dramatic difference at short scattering vectors. By measureing F^e at small scattering vectors one may therefore determine f(r) with great accuracy.

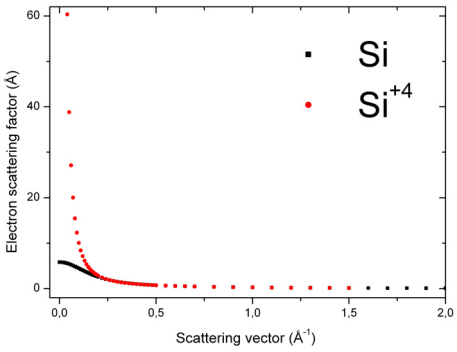

Figure 4.4: *Electron scattering factor for Silicon for a neutral atom (black) and an atom where all the valence electrons are removed (red).*

Convergent Beam Electron Diffraction (CBED) is such a technique that may determine F^e accurately [5, 6, 7]. In a CBED experiment the electron probe is focused on a crystal grain in the μm region (fig. 4.5). The probe diameter can be in the sub-nanometer region enabling the possibility of looking at small areas free of defects. Each reflection in reciprocal space will now give rise to a disc. Due to the small probe size each point within the disc will correspond to the same thickness. Great accuracy arises from this technique as each disc contains information from a large number of incident beam directions, and a lot of information can then be collected from one single pattern.

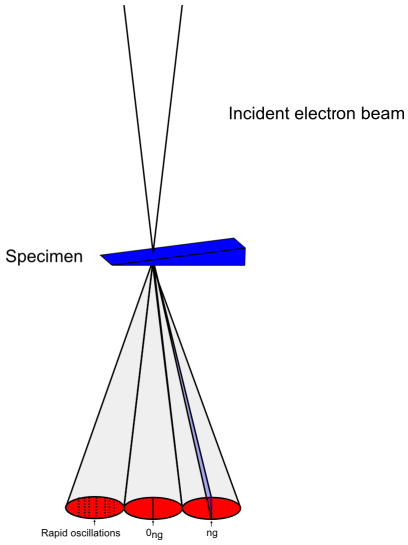

Figure 4.5: *Convergent Beam Electron Diffraction. The label ng indicates where the Bragg condition is fulfilled (0_{ng} is the corresponding deficiency line in the central disc)*

Fig. 4.6 shows a CBED image and a Bloch wave simulation of the hhh-row of Mg_2Si. To the left in fig. 4.7 a linescan along the image is shown, along with a Gaussian smearing of the linescan. This Gaussian smearing was used as background for the experiment. To the right in fig. 4.7 a Bloch wave simulation of the row is shown in addition to a linescan of the experiment when the background is subtracted. The Bloch wave simulation was done using structure factors calculated by density functional theory (DFT). Close to the overlapping areas of each disc a poor fit is achieved due to the background from the overlapping areas. The line scan in the experiment is taken outside the overlapping areas, however, some background from the overlapping areas will still be present. By comparing the structure factors calculated by DFT with experiments, the accuracy of DFT calculations may be tested. In this case a good fit between DFT calculated structure factors and experiment was achieved as the position of the peaks in the simulation fits the experiment very well.

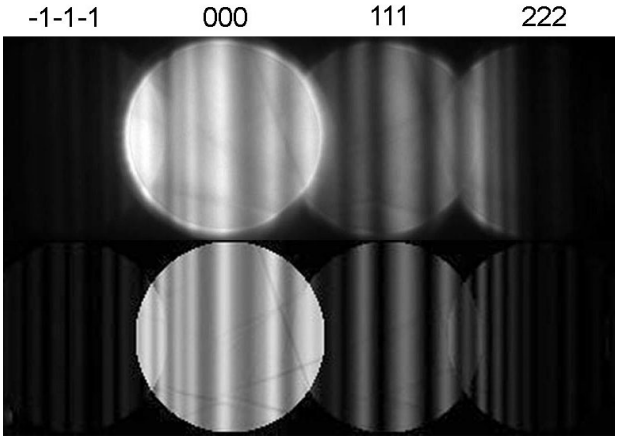

Figure 4.6: *Upper picture shows a CBED experiment along the hhh-row of Mg_2Si. Bottom picture shows a Bloch wave simulation of the hhh-row.*

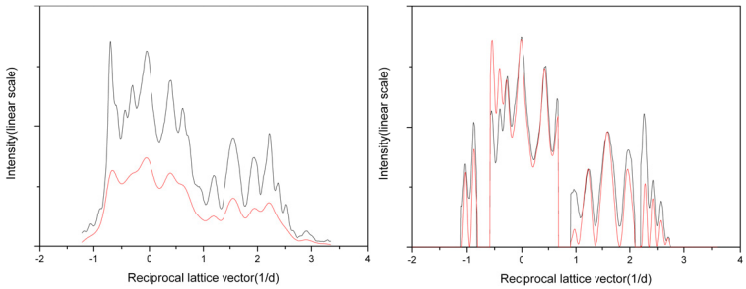

Figure 4.7: *Left picture shows a linescan of the experiment in fig. 4.6 and a Gaussian smearing of the linescan. This smearing was used to simulate the background. Right picture shows the Bloch wave simulation of the hhh-row and the linescan of the experiment when the background is subtracted.*

4.3 Large angle convergent beam

In conventional CBED the diffraction discs should not overlap as the overlapping areas create background which is difficult to simulate. However, by increasing the convergence of the electron beam, several reflections will have the Bragg condition fulfilled simultaneously [8].

The Bragg condition for a cubic lattice is fulfilled at angles θ =arcsin($\frac{\sqrt{h^2+k^2+l^2}\lambda}{2a}$), where h,k,l are the Miller indices and a is the lattice parameter. As the wavelength (λ) for fast electrons is very short (0.0025nm at 200keV), the reflections will be closely spaced in reciprocal space. By using a large angle convergent beam it is therefore possible to record reflections with large reciprocal vectors. One can now collect structure factor information by comparing the shape and size of the reflections that have the Bragg condition fulfilled. The CBED experiment may achieve great accuracy when the scattering factors of the atoms are to be determined as one normally looks at low index reflections. By increasing the convergence of the electron

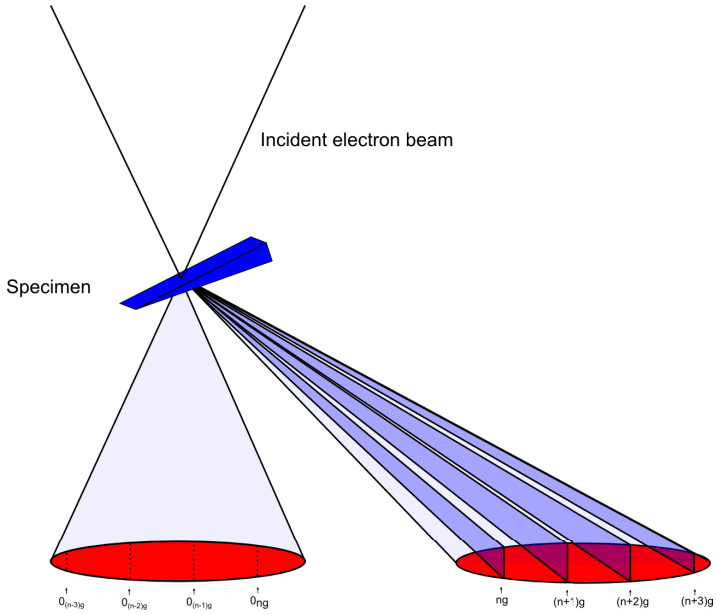

Figure 4.8: *Large angle Convergent Beam Electron Diffraction. The labels ng, 0_{ng} indicates where the Bragg condition is fulfilled and the corresponding deficiency lines in the central disc)*

beam, one may instead achieve great accuracy in determining the Debye-Waller factors of the atoms.

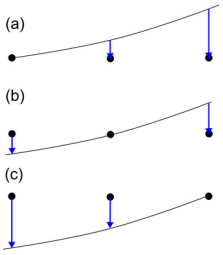

Figure 4.9: *In (a), (b) and (c), 3 reflections have the Bragg condition fulfilled. Blue arrows indicate the intensity contribution between the reflections.*

When many beams have the Bragg condition fulfilled, a reflection may get a intensity contribution from many beams simultaneously. This is illustrated in fig. 4.9, where the intensity contribution to each reflections is shown when 3 different reflections have the Bragg condition fulfilled. In a large angle scattering experiment, this will occur at reflections that are separated by a reciprocal lattice vector. This is shown in fig. 4.10 where 5 beams have the Bragg condition fulfilled simultaneously. These intensity contributions are included in the Bloch wave simulations.

Fig. 4.11 shows an experiment and simulations of the 00h row of reflections (0010-0016) on Mg_2Si. The

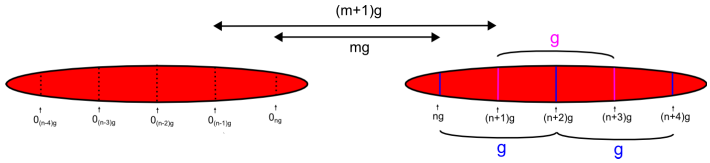

Figure 4.10: *Large angle Convergent Beam Electron Diffraction discs. The intensity contribution between every second reflection is indicated as blue and purple lines in the diffraction discs.*

position of the weak fringes around the 0012 reflection in fig. 4.11 (a) makes it possible to accurately determine sample thickness. Accurate determination is important for this specific experiment as the strong and weak reflections have very different structure factors, making the extinction distance almost three times shorter for the 0012 reflection compared to the 0016 reflection. When the intensities of the experimental peaks are compared, a flat background is chosen for all reflections. This is done as the background make up the same proportion of all reflections (as seen in the inset in fig. 4.11 (a)).

In fig. 4.11 (b) simulations of diffraction patterns using the structure factor for the procrystal and structure factor found by DFT are shown. The change in the intensity for the 0010 reflection is due to dynamical coupling between the reflections. Three simulations with different B-factors for Mg-atoms (10 $\%$ increase) and Si-atoms (10 $\%$ increase) are shown in fig. 4.11 (c) and relatively large changes in intensities are found at these small variations in B-factors.

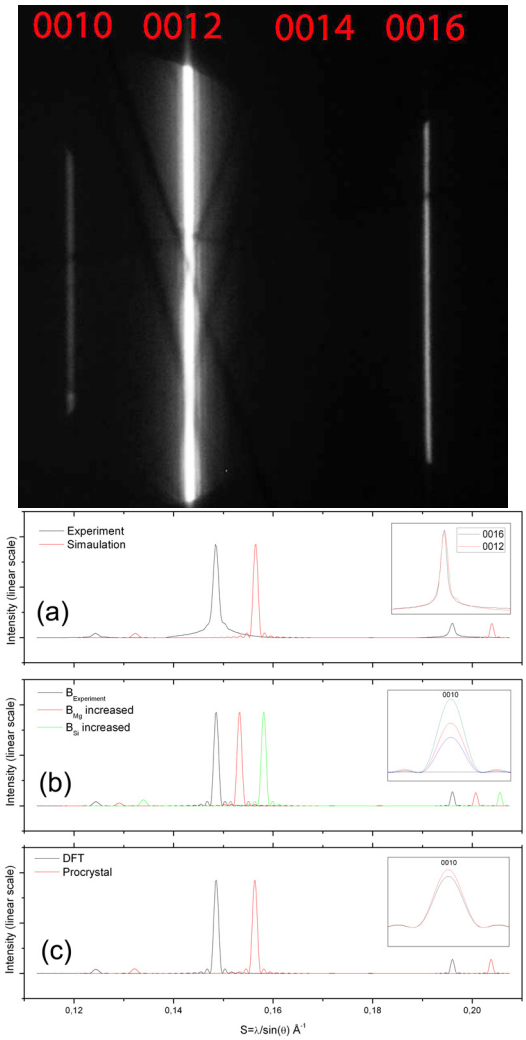

Figure 4.11: *On top a systematic row of reflections along the 00h-row on Mg_2Si is shown. (a) Linescan of the experiment and a simulation. Inset shows the normalized experimental 0012 and 0016 reflections and it is seen that the shapes of the peaks are identical. (b) Simulation of the experiment and two simulation with 10 % increase in the B factor for Silicon or Magnesium. The inset shows the change in intensity for the 0010 reflection. (c)Two simulations with different structure factor for the 002 reflection. One is using the procrystal and other is found by DFT. The inset shows the change in intensity for the 0010 reflection. The peaks are shifted to the right for peak height comparison.*

Bilbliography

[1] A. Howie. Modern diffraction and imaging techniques in material science. *(edited by S.Ãmelinckx, R. Gevers, G. Remaut and J. Van Landuyt),Nort-Holland*, page 295, 1970.

[2] M. Kogiso and H. Takahashi. Group-theoretical method in the many-beam theory of electron diffraction. *Journal of the Physical Society of Japan*, 42(1), 1977.

[3] A. Fukuhara. Many-ray approximation in the dynamical theory of electron diffraction. *Journal of the Physical Society of Japan*, 21(12):2645–2662, 1966.

[4] J. Gonnes and J. Tafto. Bloch wave symmetry in electron diffraction. *Ultramicroscopy*, 52(3-4):445–453, 1993. cited By (since 1996) 2.

[5] J. M. Zuo, M. O'Keeffe, P. Rez, and J. C. H. Spence. Charge density of mgo: Implications of precise new measurements for theory. *Phys. Rev. Lett.*, 78(25):4777–4780, Jun 1997.

[6] J. M. Zuo, M. Kim, M. O'Keeffe, and J. C. H. Spence. Direct observation of d-orbital holes and Cu-Cu bonding in Cu2O. *NATURE*, 401(6748):49–52, SEP 2 1999.

[7] L. Wu, Y. Zhu, T. Vogt, H. Su, J. W. Davenport, and J. Tafto. Valence-electron distribution in mgb_2 by accurate diffraction measurements and first-principles calculations. *Phys. Rev. B*, 69(6):064501, Feb 2004.

[8] J. Tafto and T. H. Metzger. Large-angle convergent-beam electron-diffraction-A simple technique for the study of modulated structures with application to V2D. *Journal of applied Crystallographie*, 18(APR):110–113, 1985.

Chapter 5

Materials

5.1 Mg_2Si

Mg_2Si has a fluorite structure (space group Fm-3m) with a lattice parameter of 6.338 Å. The Si atoms are placed in a cubic face centered arrangement and the Mg atoms occupy all tetrahedral positions (fig. 5.1).

The thermoelectric figure of merit of nondoped n-type Mg_2Si is poor with a maximum around 0.05 at 850 K. By doping with Sb and Bi, a large increase in the electrical conductivity and Seebeck coefficient has been found. Simultaneously, the lattice contribution to the thermal conductivity is lowered, leading to a large increase in the figure of merit with zT higher than 0.5 and 0.8 at 850 K [1, 2]. The results from pure Mg_2Si, and Mg_2Si doped with Bi are shown in fig. 5.2.

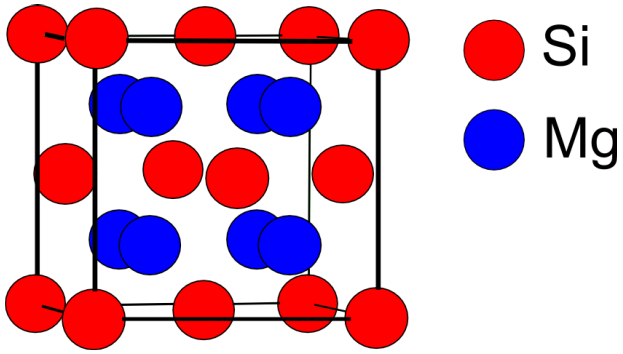

Figure 5.1: *The cubic unit cell of Mg2Si (lattice parameter=6.338 Å) consisting of face centered Si atoms and Mg atoms at tetrahedral positions.*

Electronic structure calculations on the bonding in Mg_2Si have indicated mixed covalent-ionic bond be-

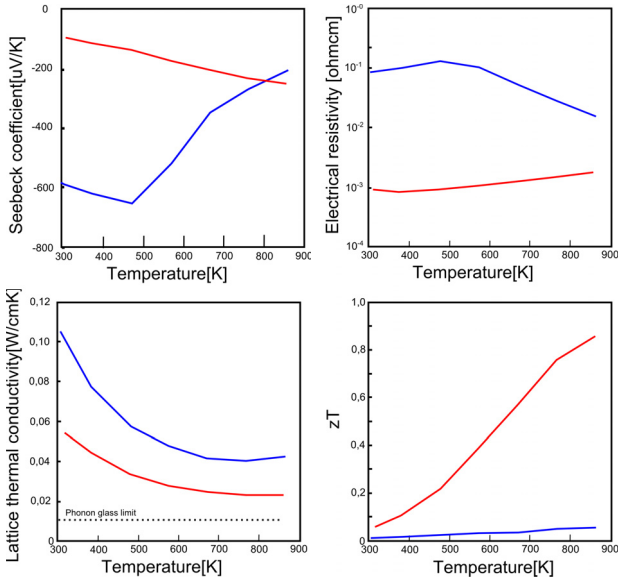

Figure 5.2: *Thermoelectric properties of polycrystalline undoped (blue) and Bi-doped (red) Mg_2Si. Adapted from ref. [3]. The phonon glass limit is calculated from the sound velocities found in ref. [4].*

tween the Mg and Si atoms [5, 6, 7]. The anharmonicity of the Mg atom along with the B factors of the Mg and Si atoms have also been studied earlier and an anharmonic parameter of -2.39x10^{-12}erg$Å^{-3}$ was found [8, 3]. Based on measured sound velocities [4], the phonon glass limit was calculated to be 1 W/mK (fig. 5.2).

5.2 ZnSb

ZnSb has an orthorombic structure (space group P/bca) with lattice parameters 6.2016 Å, 7.7416 Å and 8.0995 Å. Zn atoms and Sb atoms both have Wyckoff position c (fig. 5.3).

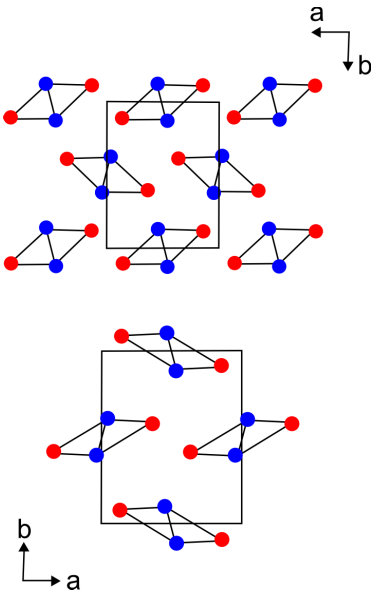

Figure 5.3: *Atomic arrangement in ZnSb, where blue are Zn atoms and red are Sb atoms [9]*

ZnSb attracted some interest several decades ago as a thermoelectric material, as ZnSb was found to be the best p-type thermoelectric material in a survey in 1950 [10]. Since then many more efficient thermoelectric materials have been discovered, like the binary phase β-Zn_4Sb_3 [11]. Recent studies found ZnSb to have a band gap of 0.3-0.5 eV [12, 13, 14]. Galvanomagnetic measurements on undoped single crystals suggest a single parabolic valence band and with general ellipsoids for surfaces of constant energy [12].

Various elements (Ag, Au, Sn and Pb) have been used as acceptor dopants in single crystal ZnSb [15]. Especially silver was found to be a good dopant as it had a high solubility in ZnSb, increasing the electrical conductivity. The thermal conductivity and figure of merit of ZnSb and Zn_4Sb_3 are shown in fig. 5.4. It can be seen that ZnSb has a higher zT than Zn_4Sb_3 at low temperatures, even if the thermal conductivity is more than two and a half times higher. By reducing the lattice thermal conductivity in the thermally more stable ZnSb phase, its figure of merit could be comparable to that found for Zn_4Sb_3.

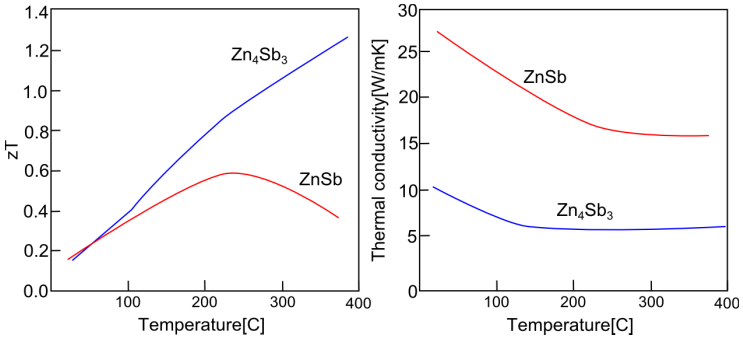

Figure 5.4: *Figure of merit and thermal conductivity of ZnSb and Zn_4Sb_3 [11] (The curve for ZnSb is shown 34.6 % zinc, 64.3 % antimony, 1 % tin and 0.1 % silver [16]). The figure of merit in Zn_4Sb_3 is higher, due to the low thermal conductivity.*

Bilbliography

[1] Jun ichi Tani and Hiroyasu Kido. Thermoelectric properties of sb-doped mg2si semiconductors. *Intermetallics*, 15(9):1202 – 1207, 2007.

[2] J. Tani and H. Kido. Thermoelectric properties of bi-doped Mg2Si semiconductors. *Physica B-Condensed matter*, 364(1-4):218–224, JUL 15 2005.

[3] M. J. Cooper and D. Panke. Anharmonic thermal vibrations in Mg2Si. *Acta crystallographica section A-Crystal physics diffraction theoretical and general crystallography*, A 26:292–&, 1970.

[4] W. B. Whitten, P. L. Chung, and G. C. Danielson. Elastic constants and lattice vibration frequencies of mg2si. *Journal of Physics and Chemistry of Solids*, 26(1):49 – 56, 1965.

[5] P. Baranek, J. Schamps, and I. Noiret. Ab Inito Studies of Electronic Structure, Phonon Modes, and Elastic Properties of Mg_2Si. *J. Phys. Chem. B*, 101:9147, 1997.

[6] P. Baranek and J. Schamps. Influence of Electronic Correlation and Structural, Dynamic and Elastic Properties of Mg_2Si. *J. Phys. Chem. B*, 102:2601, 1999.

[7] B. Yu, D. Chen, Q. Tang, C. Wang, and D. Shi. Structural, electronic, elastic and thermal properties of Mg_2Si. *J. Phys. Chem. Solids*, 71:758, 2010.

[8] D. Panke and E. Wolfel. Distribution of valence electrons in Mg2Si. *Zeitschrift fur Kristallographie Kristallgeometrie Kristallohysik Kristallchemie*, 129(1-4):9–&, 1969.

[9] A. S. Mikhaylushkin, J. Nylen, and U. Haussermann. Structure and bonding of zinc antimonides: Complex frameworks and narrow band gaps. *Chemistry-A european journal*, 11(17):4912–4920, AUG 19 2005.

[10] M. Telkes. Thermoelectric power and electrical resistivity of minerals. *American mineralogist*, 35(7-8):536–555, 1950.

[11] G. J. Snyder, M. Christensen, E. Nishibori, T. Caillat, and B. B. Iversen. Disordered zinc in Zn4Sb3 with phonon-glass and electron-crystal thermoelectric properties. *NATURE Materials*, 3(7):458–463, JUL 2004.

[12] P. J. Shaver and J. Blair. Thermal and electronic transport properties of p-type znsb. *Phys. Rev.*, 141(2):649–663, Jan 1966.

[13] N. F. Mott. Electrons in disordered structures. *Advances in Physics*, 50(7):865–945, 2001.

[14] L. T. Zhang, M. Tsutsui, K. Ito, and M. Yamaguchi. Effects of znsb and zn inclusions on the thermoelectric properties of [beta]-zn4sb3. *Journal of Alloys and Compounds*, 358(1-2):252 – 256, 2003.

[15] N. L. Kostur and V. I. Psarev. Electrical properties of alloyed ZnSb single crystals. *Izvestiya vysshikh uchebnykh zavedenii fizika*, (2):39–&, 1967.

[16] R. R. Heikes and R. W. Ure Jr. *Thermoelectricity: Science and Engineering*. Interscience Publishers New York-London, 1961.

Chapter 6

Summary of papers

6.1 Paper I

Bloch wave symmetries in electron diffraction:
Applications to Friedels law, Gjonnes-Moodie lines and refraction at interfaces
K. Valset and J. Taftø
Ultramicroscopy 7, 854-859 (2011)

This paper was written on the occasion of Prof. John Spence's 65th birthday. In an earlier unpublished work, Johan Taftø had classified the symmetries of the 17 two-dimensional space groups. In this paper we publish these symmetries and give some examples of application. It is shown that by utilizing symmetries of an infinite row of reflections, refraction/reflection of fast electrons at interfaces may be calculated. Simulations are done to confirm the results from these symmetry considerations for a systematic row of reflections.

6.2 Paper II

Electronic structure of Mg_2Si by combining electron diffraction and first-principle calculations
K. Valset, E. Flage-Larsena, P. Stadelmann and J. Taftø
Submitted to Acta Materialia

Silicides have attracted a lot of interest for thermoelectric studies as they consists of cheap, nontoxic elements. In this paper we study the atomic bonding in the silicide Mg_2Si, as it upon doping has been shown to have good thermoelectric properties. The atomic bonding in Mg_2Si has been studied earlier using X-ray diffraction, however, the bonding has not been studied by electron diffraction earlier. We therefore used convergent beam electron diffraction (CBED) to determine the structure factor of the reflections most sensitive to bonding (i.e. the 002 reflection and 111 reflection). The experiment was simulated using the Bloch wave program incorporated in the JEMS software by P. Stadelmann. Density functional theory (DFT) calculations of the bonding in Mg_2Si was done by E. Flage-Larsen. The structure factors found from the DFT calculations were then compared to the CBED experiments. Some disagreement was found between the structure factors found by CBED in this work and earlier X-ray diffraction experiments. The accuracy in a CBED experiment at short reciprocal vectors is superior to X-ray diffraction experiments, as indicated by the excellent agreement between DFT calculations and CBED experiment in this work. CBED is therefore found to be an important complementary technique to X-ray diffraction.

6.3 Paper III

Precision electron diffraction measurements of anharmonic thermal motion of atoms
K. Valset, J. Taftø, L. Wu and Y. Zhu
Submitted to Physical Review Letters

In this paper we continue the study of the silicide Mg_2Si, with emphasis on atomic thermal vibrations. The B-factors of Mg and Si and the anharmonic vibrations of the Mg atoms are measured earlier by X-ray diffraction. Here we use electron diffraction and utilize the short wavelength of the fast electrons to study reflections at large reciprocal vectors. Part of this work was done at Brookhaven National Laboratory in collaboration with Yimei Zhu and Lijun Wu. The Bloch wave simulation program developed by Lijun proved useful for simulations of systematic rows of reflections. Larger deviations were found for the B factors than for the anharmonic paramet, possibly because these parameters are more sensitive to heating by the electron beam that occurs in the crystal.

6.4 Paper IV

Thermoelectric properties of Cu doped p-type ZnSb containing Zn_3P_2 particles
K. Valset, P. H. M. Bottger, J. Taftø and T. Finstad
Submitted to Journal of Applied Physics

Motivated by the excellent properties of β-Zn_4Sb_3 we try in this work to optimize the thermoelectric properties of the thermally more stable ZnSb phase. Optimization was done by forming particles of Zn_3P_2 inside ZnSb to lower the thermal conductivity. A reduction in thermal conductivity up to 15 $\%$ was achieved in this way. Additional doping of copper was done to increase the carrier concentration. Most electrical measurements were done by P.H.M. Bottger and this paper take advantage of his earlier work on copper doped ZnSb. A considerable improvement in the thermoelectric figure of merit was found. Interestingly, this improvement may be associated with the electronic properties of the nanoparticles, resulting in modulation doping.

Paper I

K. Valset and J. Taftø
Bloch wave symmetries in electron diffraction:
Applications to Friedels law, Gjonnes-Moodie lines
and refraction at interfaces
Ultramicroscopy **7**, 854-859 (2011)

Paper II

K. Valset, E. Flage-Larsena, P. Stadelmann and J. Taftø
Electronic structure of Mg_2Si by combining
electron diffraction and
first-principle calculations
Submitted to Acta Materialia

Electronic structure of Mg_2Si by combining electron diffraction and first-principle calculations

K.Valset[a,1], E.Flage-Larsen[a], P.Stadelmann[b], J.Taftø[a]

[a] *Department of Physics, University of Oslo, Blindern P.O. Box 1048, 0316 Oslo, Norway*
[b] *École Polytechnique Fédérale de Lausanne, CIME, CH-1015 Lausanne, Switzerland*

Abstract

We have used accurate convergent beam electron diffraction (CBED) to determine the structure factors of the reflections most sensitive to the valence-electron distribution in Mg_2Si. The experimental values agree well with calculations of the structure factors based on density functional theory. Based on the experimentally scrutinized electron structure calculations we show that this promising thermoelectric material is highly ionic, arriving at the charge $Mg_2^{1.45+}Si^{2.9-}$.

1. Introduction

Thermoelectricity is interesting for a large number of applications due to the simplicity and reliability of thermoelectric devices. The hindrance for widespread use of thermoelectric heat-pumps and electricity generators is the low efficiency of the materials involved. Increasing the thermoelectric figure of merit of low cost thermoelectric materials is therefore an area of great scientific effort. Promising thermoelectric materials possess low thermal conductivity, good electrical conductance and a high Seebeck coefficient. These properties are interdependent and difficult to optimize individually. Except for lattice thermal conductivity and the electron-phonon coupling, the thermoelectric properties of materials are determined by the band structure and the electron-electron scattering mechanisms. Detailed knowledge of the band structure and electron-electron coupling is therefore important. What is particularly interesting is the

[1] Email: kjetil.valset@fys.uio.no, Tlf: +47 228 40662, Fax: +47 22 05 06 51

strong correspondence between the band structure, the bonding and geometric structure of the compound. It should thus, ultimately be possible to predict optimum band structures for high-performance thermoelectric materials based on detailed knowledge of the bonding and symmetry of the material. The bonds in molecules and crystals are governed by a favorable energetic rearrangement of the valence electron distribution and studies of this rearrangement can yield additional insight and assist in future predictions of better thermoelectric materials.

Convergent beam electron diffraction is a direct way of experimentally testing electronic structure calculations of crystals [1]. By accurately determining the structure factors of a crystal, information regarding the valence-electron distribution can be found. The aim of this work is to combine electron diffraction and density functional theory calculations(DFT) to investigate the bonding in the Mg_2Si compound and validate the calculations. The Mg_2Si compound is considered a promising high-performance thermoelectric material. It has a cubic structure with $Fm\bar{3}m$ symmetry (see Fig. 1). Previous X-ray diffraction studies and electronic structure calculations on this material suggested a mixture of covalent and ionic character [2, 3, 4].

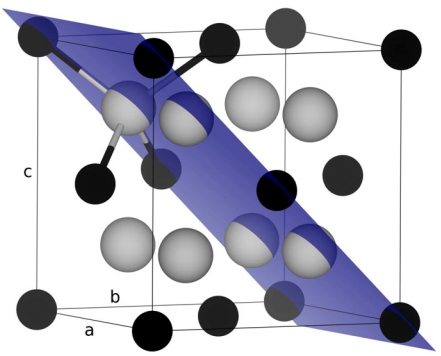

Figure 1: The ground state of Mg_2Si with $Fm\bar{3}m$ symmetry. Magnesium and silicon atoms are gray and black respectively. The (011) plane is shown.

In this work we have used precision electron diffraction to determine the structure factors of the reflections most sensitive to changes in the electron density. Using electron diffraction these are generally the structure factors associated with short g-vectors. In this particular case, dealing with the fcc crystal Mg_2Si, these are the 111 and 200 reflections.

2. Methodology

2.1. Electron diffraction and structure factors

In diffraction experiments the fast electrons interact electrostatically with the electrons and nucleus of the atoms. For Mg_2Si, a large relative change in the electron distribution may be expected as both Si ($Z = 14$) and Mg ($Z = 12$) are light elements. Thus, the valence electrons engaged in bonding are a substantial fraction of the total number of electrons leading to a large change in the structure factors compared to the procrystal values [5]. The procrystal is a superposition of the overlapping free atomic valence electron densities. The X-ray scattering factor, $f^{(x)}$ may be converted to the electron scattering factor, $f^{(e)}$ by use of the Mott formula:

$$f^{(e)} = c\frac{Z - f^{(x)}(S)}{S^2},$$

where c is a constant and S is the scattering vector. At short reciprocal vectors the X-ray scattering factor approach the number of electrons around the atoms. From the Mott formula it is therefore evident that if $S \to 0$, a small perturbation in $f^{(\mathrm{x})}$ yields a large change in $f^{(\mathrm{e})}$. Electron diffraction may thus achieve better accuracy for determination of the low order structure factors (small S) as compared to X-ray diffraction.

The electron diffraction experiments were done at room temperature with 200 kV electrons using a JEOL 2010 with a Gatan Imaging Filter. In a CBED experiment the electron probe is focused on a grain with size in the micrometer range. The Debye-Waller factors used was taken from ref. 6 . The diffraction disc simulations were done with Bloch waves using the JEMS program [7]. Most diffraction patterns were taken at thicknesses ranging from 350 nm to

500 nm. Though absorption of fast electrons is more severe as the thickness increases, the features within the CBED discs will be more sensitive to changes in the structure factor. One also avoids bending of the crystal that occures at thinner areas. Simulations using different scattering factors [8, 9] resulted in no significant difference. When absorption is disregarded, the intensity of a reflection **g** is given by:

$$I_{\mathbf{g}}(z) = \sum_{j} \sum_{j'} C_0^{(j)} C_g^{(j)} C_0^{(j')*} C_g^{(j')*} e^{2\pi i(\gamma^j - \gamma^{j'})z}$$

where C_g^j and γ^j are the Bloch wave coefficient and anpassung associated with Bloch wave j. z is the thickness. From the above expression it is evident that rapid oscillations in the intensity will occur when the differences between the anpassungen are large (i. e. at reflections that are not in Bragg). These oscillations are very sensitive to variation in thickness and it was thus possible to determine the thickness with an accuracy of a few nm.

2.2. Background subtraction

Diffuse scattering creates a background within the electron diffraction discs. The background was taken into account by applying a Gaussian smearing of a scan along the discs in the 00h-row and hhh-row. The diffraction discs have some overlapping areas, making a contribution to the background not considered along this scan. The resulting curve was then subtracted from the experiment. This approach may give some deviations regarding the amplitudes of the oscillations within the discs. However, as the experiments were taken at thick areas of the sample, accurate values for the structure factors can be collected from the position of the maxima and minima of the oscillations.

2.3. Density functional theory and structure factors

Density functional theory (DFT) calculations were based on the Perdew–Burke–Ernzerhof (PBE-GGA) [10] exchange–correlation functional. The projector–augmented–wave (PAW) [11, 12] method was employed. All calculations were

done using the Vienna Ab–initio Simulation Package (VASP) [13, 14]. An energy cutoff and k-point sampling of 550 eV and 12×12×12, respectively was used.

The all-electron valence density was determined in a second run on a denser electron density grid where the electron density difference (EDD) was calculated by taking the difference $\rho_{\mathrm{EDD}} = \rho_{\mathrm{c}} - \rho_{\mathrm{p}}$ of the all-electron valence density of the crystal ρ_{c} and the procrystal ρ_{p}. A positive EDD corresponds to an accumulation of electrons, while the opposite yields depletion of electrons. This is a convenient and straightforward way of obtaining quantitative spatial bonding data [15, 16, 17]. The calculated X-ray structure factors $F^{(\mathrm{x})}_{\mathrm{DFT}}$ is obtained by a Fourier transform of the electron density. Since $F^{(\mathrm{x})}_{\mathrm{DFT,EDD}} = F^{(\mathrm{x})}_{\mathrm{DFT,c}} - F^{(\mathrm{x})}_{\mathrm{DFT,p}}$, calculating the EDD equivalent for the X-ray structure factors is trivial and static core contributions disappears. To obtain quantitative electron transfer we performed Bader analysis [18] which assigns electron charge to atoms by means of a zero flux surface.

3. Results and discussion

Fig. 2 shows a simulation of the $00h$-row of reflections for the procrystal, the experiment and a simulation of the row using the structure factors calculated by DFT. These simulations are at the same thickness. Similarly, in Fig. 3 the corresponding results for the hhh-row are presented. In both cases a large change is found between the simulation of the diffraction discs for the procrystal and DFT calculations, indicating the sensitivity of this method.

The bottom of Fig. 2 and Fig. 3 show line scans of the experiments where the background is subtracted and of the simulation using the DFT values. The experimental amplitudes matched the simulations reasonably well for the $00h$-row, but less so for the hhh-row as larger parts of the diffraction discs overlapped. The line scan was taken outside the overlapping areas but some additional background from the overlapping areas is present. However, in both cases the position and width of the oscillations matched the experiment very well.

Table 1: X-ray structure factors for the procrystal $F_{\mathrm{p}}^{(\mathrm{x})}$, the electron diffraction experiment $F_{\mathrm{exp}}^{(\mathrm{x})}$ and the DFT calculations $F_{\mathrm{DFT}}^{(\mathrm{x})}$.

Reflection	$F_{\mathrm{p}}^{(\mathrm{x})}$	$F_{\mathrm{exp}}^{(\mathrm{x})}$	$F_{\mathrm{DFT}}^{(\mathrm{x})}$
002	-32.07	-31.13 ±0.40	-31.13
111	43.96	45.27 ±0.25	45.09

Table 2: The fourier potential in volts at 200 keV for the procrystal $V_{\mathrm{p}}^{(\mathrm{x})}$, the electron diffraction experiment $V_{\mathrm{exp}}^{(\mathrm{x})}$ and the DFT calculations $V_{\mathrm{DFT}}^{(\mathrm{x})}$.

Reflection	$V_{\mathrm{p}}^{(\mathrm{e})}$	$V_{\mathrm{exp}}^{(\mathrm{e})}$	$V_{\mathrm{DFT}}^{(\mathrm{e})}$
002	-1.81	-2.05 ±0.10	-2.05
111	3.83	3.39 ±0.09	3.45

The DFT calculations indicate a change in the structure factor of several percent for the most sensitive reflections and are displayed in Table 1 and 2. Table 1 gives the XRD structure factor values for the procrystal $F_{\mathrm{p}}^{(\mathrm{x})}$, the experiment $F_{\mathrm{exp}}^{(\mathrm{x})}$ and DFT $F_{\mathrm{DFT}}^{(\mathrm{x})}$. Table 2 lists their corresponding Fourier potential. By comparing these values it is clear that the relative change in $F^{(\mathrm{e})}$ between experiment and procrystal is much larger than for $F^{(\mathrm{x})}$. This illustrates the increased sensitivity to valence electron distribution at short scattering vectors using electron diffraction.

Given the good agreement between experiment and DFT it is reasonable to assume that the ground state electron density of Mg_2Si is well described within the DFT framework used in this work. It is thus interesting to investigate the bonding character of the Mg-Si network based on these calculations. In Fig. 4 we give the electron density and the EDD in the (011) plane. Even though there is some directional electron transfer between the Mg and Si atom, it is clear that the ionic character dominates, where Si accumulate electrons from Mg. A small rearrangement is seen in the Si orbitals to account for the large electron accumulation. The ionicity of the Si-Mg bond is also confirmed in Table 3 where valence electron occupation numbers are given based on Bader analysis. Here, Mg lose almost one and a half electron (occupation number of 0.55) compared to its valence electrons in the non-bonding state, while the Si atoms accumulate the majority of this depletion, resulting in an occupation number of 6.91. Thus,

Table 3: Electron occupation numbers for Mg and Si extracted from Bader analysis.

	Valence electrons		
	Free atom	Crystal	Difference
Mg	2.00	0.55	-1.45
Si	4.00	6.91	+2.91

Table 4: The most bond sensitive structure factors $F^{(x)}_{\mathrm{DFT,EDD}}$ calculated by the use of density functional theory. The largest change is for the 111 and 200 structure factor and they rapidly decay for larger scattering vectors.

	$F^{(x)}_{\mathrm{DFT,EDD}}$
111	1.384
200	0.960
220	0.676
311	0.640
222	0.402
420	0.249
422	0.237
440	0.204
620	0.132
444	0.108

Si gain almost three electrons in this structure, in accordance with the two to one ratio between Mg and Si. In the present study we arrive at an electron distribution of $Mg^{1.45^+}Si^{2.9^-}$. Previous calculations based on linear combination of atomic orbitals (LCOA) [3, 4] suggest $\mathrm{Mg}^{0.9^+}\mathrm{Si}^{1.8^-}$, while a complete exchange-correlation calculation resulted in $\mathrm{Mg}^{0.65^+}\mathrm{Si}^{1.3^-}$. These discrepencies may be partly attributed to the different ways of assigning charges to the ions. A more precise way of comparing DFT calculations is to compare the resulting X-ray structure factors. Results from our DFT calculations are shown in Table 4.

Our calculations are qualitatively similar to the previous all-electron DFT calculation [4], but quantitatively different due to the artifical localization of the LCAO basis set, yielding a lower ionicity. Additional studies suggest that the electron mainly accumulate around the Si atoms [19, 20] but do not give quantitative data. Our analysis predicts semi-local electron transfer, which is difficult to obtain with a LCAO basis set and subsequent Mulliken analysis, and

we thus believe it to be more accurate.

3.1. Summary and outlook

Electron diffraction measurements of the bond sensitive structure factors of Mg_2Si were performed and compared to density functional theory calculations. Excellent agreement was found. Electron diffraction is a complementary technique to X-ray diffraction as the structure factors with short scattering vectors are strongly influenced by the valence electron distribution. Thus, as demonstrated in this work, precision electron diffraction offers a sensitive way of validating density functional theory calculations.

[1] J. M. Zuo, M. OKeeffe, P. Rez, and J. C. H. Spence. Charge density of MgO: Implications of precise new measurements for theory. *Physical Review Letters*, 78(25):4777–4780, JUN 23 1997.

[2] R. Saravanan and M. C. Robert. Local structure of the thermoelectric material Mg2Si using XRD. *Journal of Alloys and Compounds*, 479(1-2):26–31, JUN 24 2009.

[3] P. Baranek, J. Schamps, and I. Noiret. Ab Inito Studies of Electronic Structure, Phonon Modes, and Elastic Properties of Mg_2Si. *J. Phys. Chem. B*, 101:9147, 1997.

[4] P. Baranek and J. Schamps. Influence of Electronic Correlation and Structural, Dynamic and Elastic Properties of Mg_2Si. *J. Phys. Chem. B*, 102:2601, 1999.

[5] L. J. Wu, Y. M. Zhu, T. Vogt, H. B. Su, J. W. Davenport, and J. Taftø. Valence-electron distribution in MgB2 by accurate diffraction measurements and first-principles calculations. *Physical Review B*, 69(6), FEB 2004.

[6] D. Panke and E. Wolfel. Distribution of Valence Electrons in Mg2Si. *Zeitschrift fur Kristallographie Kristallgeometrie Kristallphysik Kristallchemie*, 129(1-4):9–&, 1969.

[7] P. Stadelmann. *Microsc. and Microanal.*, 9,Suppl. 3:60, 2003.

[8] L. M. Peng, G. Ren, S. L. Dudarev, and M. J. Whelan. Debye-Waller factors and absorptive scattering factors of elemental crystals. *Acta Crystallographica Section A*, 52(Part 3):456–470, MAY 1 1996.

[9] A. Weickenmeier and H. Kohl. Computation of Absorptive Form-Factors for High-Energy Electron.Diffraction. *Acta Crystallographica Section A*, 47(Part 5):590–597, SEP 1 1991.

[10] J. P. Perdew, K. Burke, and M. Ernzerhof. *Phys. Rev. Lett.*, 77:3865, 1996.

[11] P. E. Blöchl. *Phys. Rev. B*, 50:17953, 1994.

[12] G. Kresse and D. Joubert. *Phys. Rev. B*, 59:1758, 1999.

[13] G. Kresse and J. Hafner. *Phys. Rev. B*, 48:131158, 1993.

[14] G. Kresse and J. Hafner. *Phys. Rev. B*, 49:14251, 1994.

[15] E. Flage-Larsen, O. M. Løvvik, Ø Prytz, and J. Taftø. *Comp. Mater. Sci.*, 47:752, 2010.

[16] E. S. Toberer, A. F. May, B. C. Melot, E. Flage-Larsen, and G. J. Snyder. Electronic structure and transport in thermoelectric compounds azn_2sb_2 (a = sr, ca, yb, eu). *Dalton T.*, 39:1046, 2010.

[17] A. Zevalkink, E. S. Toberer, W. G. Zeier, E. Flage-Larsen, and G. J. Snyder. *Energy Environ. Sci.*, 4:510, 2011.

[18] W. Tang, E. Sanville, and G. Henkelman. A grid-based Bader analysis algorithm without lattice bias. *Journal of Physics-Condensed Matter*, 21(8), FEB 25 2009.

[19] D. M. Wood and A. Zunger. Electronic structure of generic semiconductors: Antifluorite silicide and III-V compounds. *Phys. Rev. B*, 34:4105, 1986.

[20] B. Yu, D. Chen, Q. Tang, C. Wang, and D. Shi. Structural, electronic, elastic and thermal properties of Mg_2Si. *J. Phys. Chem. Solids*, 71:758, 2010.

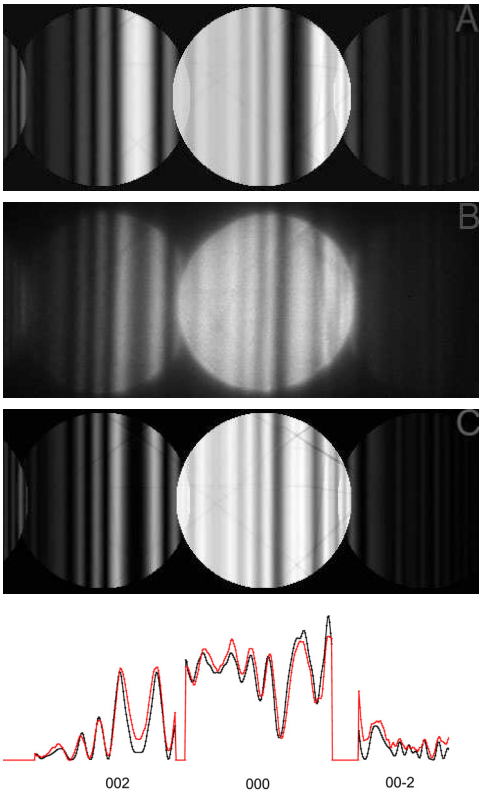

Figure 2: Diffractorgrams of the $00h$-row of reflections in Mg_2Si for three different configurations. A is the simulated discs for the procrystal, B is the experiment and C is simulated discs based on the DFT calculations. At the bottom a linescan of B(red line) and C is shown.

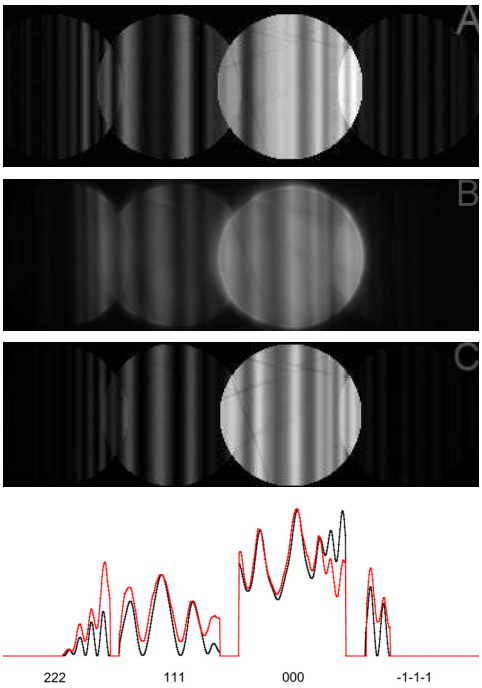

Figure 3: Diffractorgrams of the *hhh*-row of reflections in Mg_2Si for three different configurations. A is the simulated discs for the procrystal, B is the experiment and C is simulated discs based on the DFT calculations. At the bottom a linescan of B(red line) and C is shown.

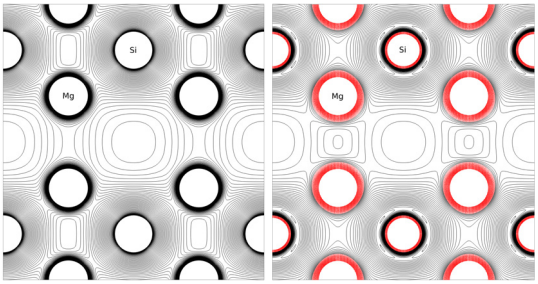

(a) Electron density (b) Electron density difference

Figure 4: (Color online) Electron density (a) and electron density difference (EDD) (b) in the (011) plane of Mg_2Si. The electron density is given from 0 to 0.1 bohr/Å. For the EDD, electron accumulation is shown in black (0 to 0.1 bohr/Å), while depletion is shown in red (-0.1 to 0 bohr/Å). All contours are given in 0.002 increments.

Paper III

K. Valset, J. Taftø, L. Wu and Y. Zhu
Precision electron diffraction measurements
of anharmonic thermal motion of atoms
Submitted to Physical Review Letters

Precision electron diffraction measurements of anharmonic thermal motion of atoms

K. Valset* and J. Taftø

Department of Physics, University of Oslo,

Blindern P.O. Box 1048, 0316 Oslo, Norway

L. Wu and Y. Zhu

Materials Science Division, Brookhaven National Laboratory, Upton, NY11973, USA

Abstract

We study the thermal motion of the atoms in the thermoelectric material Mg_2Si by using electron diffraction. The nanodiffraction, or convergent beam electron diffraction technique we use allows us to observe many Bragg reflections with large reciprocal lattice vectors simultaneously. Previous observations of anharmonicity by single crystal x-ray diffraction are confirmed, and we determine the anharmonicity parameter of the Mg atom in the tetrahedral environment with high accuracy, β= (-4.56±0.12)10^{-12} ergÅ^{-3} at room temperature. In an alternative picture the Mg atom tends to vibrate around positions displaced 4.37±0.15 pm from the centre of the tetrahedron.

Neutron and x-ray diffraction are established quantitative crystallographic techniques, while electron diffraction has traditionally been a qualitative technique. Convergent beam electron diffraction (CBED) offers new opportunities for electron diffraction and has in the last decade been used to study bonding in crystals by accurately measuring structure factors for short reciprocal vectors [1–3].

In this work we use CBED to study the anharmonicity of the thermal motion of atoms by accurately measuring structure factors for large reciprocal vectors. We study the promising thermoelectric material Mg_2Si [4, 5] in order to gain insight into the phonon contribution to the thermal conductivity. High energy efficiency of a thermoelectric material requires a large dimensionless figure of merit given by $\frac{\alpha^2}{\gamma L}$. Here α is the Seebeck coefficient, L is the Lorenz number, $\gamma = \frac{\kappa_e+\kappa_{ph}}{\kappa_e}$ where κ_{ph} is the phonon contribution and κ_e the electronic contribution to the thermal conductivity. Reducing γ by reducing the phonon contribution to the thermal conductivity increases the fig-

*Electronic address: kjetil.valset@fys.uio.no

ure of merit. Umklapp scattering is a result of anharmonicity and is important in reducing κ_{ph} at high temperatures. Thus, observations and measurements of anharmonicity may contribute in the development of strategies for more energy efficient thermoelectric materials. In a wider perspective, this nanodiffraction technique may become powerful in studying the local thermal properties of polycrystalline, including microcrystalline and nanostructured, materials through accurate measurements of structure factors at large reciprocal vectors.

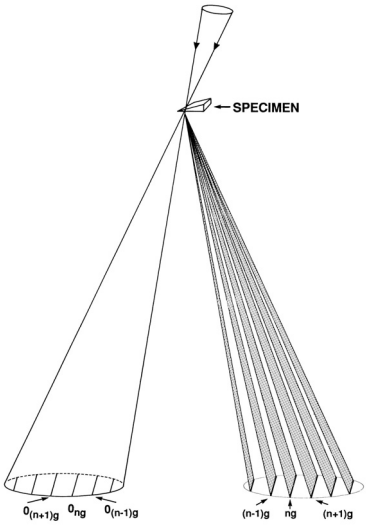

FIG. 1: By using a large angle convergent beam, many reflections (g) have the Bragg condition fulfilled simultaneously. Taken from ref. 6.

Mg_2Si has the fluorite structure, a cubic structure with Si in a face centered cubic arrangement and the Mg atoms occupying all tetrahedral positions. Anharmonicity at the tetrahedral positions in fluorite structures was much studied around 50 years ago by single crystal x-ray and neutron diffraction. We use electron diffraction on polycrystalline materials. By focusing the electron beam, a tiny crystallite acts as a single crystal. We use a large convergent beam angle [6]. Thus, many reflections along a reciprocal lattice row may be at the Bragg

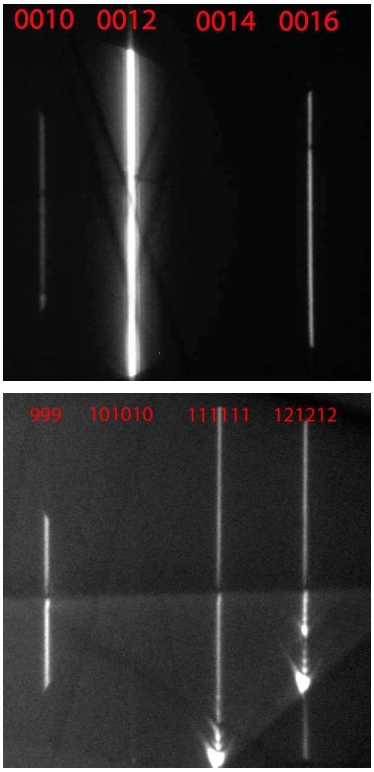

FIG. 2: Reflection along the 00h-row and the hhh-row.

position simultaneously (fig. 1). The short wavelength of the electrons results in closely spaced reflections with respect to scattering angle, making it possible to examine high index reflections. Electron diffraction may therefore be very sensitive in studying the thermal vibrations of atoms.

The experiments were done with 200 kV electrons at room temperature using a JEOL 2010 transmission electron microscope with a Gatan Imaging Filter. The reflections were recorded by a multiscan CCD camera. Fig 2 shows diffraction patterns of the 00h and hhh reciprocal row at room temperature. Experimental and simulated patterns are shown in fig. 3. The simulated patterns (shown as dotted lines) are shifted slightly to the right for peak height comparison. By normalizing the 0012 and 0016 reflections (inset fig 3 a) it is clear that the shape of the diffraction peaks including the diffuse background are the same. A simple smooth background was therefore sufficient when the intensities of the reflections are compared. Multibeam Bloch wave calculations were used to simulate the diffraction intensities. Due to the small unit cell and low Z-elements of Mg_2Si we where able to choose incident beam directions where contributions from reflections outside the systematic row were negligible. Thus, the calculations were done by including only reflections along the actual systematic row. We did the calculations with different numbers of reflections along the row and found 15 beams to be sufficient. When the 00h-row was examined the sample thickness was determined from the fringes of the 0012-reflection and was found in the region of 250nm. The strong 0012-reflection has an extinction distance of 1350 nm. The extinction distance is proportional to the inverse of the structure factor. Thus, for the weak reflections present under these experimental conditions, the diffraction patterns show only small variations with thickness.

Assuming harmonic potentials, the structure factor of Mg_2Si may be expressed as:

$$F(4n+2) = 4f_{Si}exp(-B_{Si}S^2) - 8f_{Mg}exp(-B_{Mg}S^2)$$
$$F(4n) = 4f_{Si}exp(-B_{Si}S^2) + 8f_{Mg}exp(-B_{Mg}S^2)$$
$$F(4n \pm 1) = 4f_{Si}exp(-B_{Si}S^2)$$

Using these structure factors along the 00h-row we arrive at B-factors for Mg and Si in close agreement with a previous study [7]. For the hhh row using the same B-factors we notice that the agreement between calculation and experiment is very good for the even index reflections, but not for the odd index reflections (fig 3 b). This may be explained by anharmonic vibrations of the Mg-atoms. Following the treatment of Dawson [8, 9] the structure factors for odd index reflections of fluorite structures can be expressed by intro-

ducing the anharmonic parameter β:

$$F(4n \pm 1) = 4f_{Si}exp(-B_{Si}S^2)$$
$$\pm 8f_{Mg}exp(-B_{Mg}S^2)(\frac{B_{Mg}}{4\pi a})^3\frac{hkl}{k_BT}\beta$$

Here a is the lattice parameter, which in this case is 6.338 Å. The anharmonicity does not influence the reflections when at least one of the indices in the product hkl is zero as is the case for the 00h row. By including the anharmonicity the agreement becomes excellent also for the hhh-row (fig 3 c). Experiments for different crystallites and different specimen thicknesses gave consistent results and we conclude that β= (-4.56±0.12)10^{-12} ergÅ^{-3}, B_{Mg}=0.780±0.025 Å^2 and B_{si}=0.579±0.011 Å^2. To estimate the accuracies we perform in this study several experiments in that the number of reflections is too few for R-factor calculations to be meaningful. A challenge using CBED is that we are illuminating a very thin area and small crystal volume with a rather high flux of electrons. Thus, the temperature may not be well defined and may vary some tens of degrees due to heating caused by the incident electrons. It is interesting that the B-factors varied more than the β-parameter from one experiment to the next. This is in line with the observation of ref. 9. They observed a variation in β of only 20 % between room temperature and 600^{o}C in their study of BaF_2, while the B-factors increased a factor 3 within the same temperature range. Based on single crystal X-ray diffraction data, which were originally collected for another purpose [7], a subsequent analyzis [10] concluded with β= -2.39·10^{-12} ergÅ^{-3}. Their data were for this particular purpose limited with a maximum value of the product hkl = 245. The maximum value of the product hkl in our study was 1331, suggesting a great increase in the sensitivity.

Originally another model was used by Willis [11] to describe the anharmonicity related to the vibrations of the atoms in the tetrahedral positions of fluorite structures, in the present case the Mg atoms. His description was criticized for being unphysical. In the original model of Willis the Mg atoms vibrate around positions displaced a minute distance δ in the <111> direction away from the center of the tetrahedron. The advantage of his model is that it gives a clear geometrical picture of the structure. The disadvantage is that this model does not account for the anharmonicity if one interprets the model literally because in this description the Mg atoms vibrate harmonically around the slightly displaced position. There are four such equivalent positions in the tetrahedron and their probability densities overlaps strongly due to the vibrations. Thus, this results in each Mg atom being confined within

a tetrahedral shaped region which may account for the anharmonicity. In both models three parameters are involved in describing the thermal motion of the atoms, one parameter in addition to the B-factors of the two elements of the crystal. The experimental diffraction data can be described equally well with both models as seen in fig. 4, in spite of the notion that Dawson's model is considered to be preferable, see ref. 9 for details. By the model proposed by Willis the B-factor of the Mg-atoms has to be reduced due to delocalization caused by placing the Mg atom with 25 % probability in the four equivalent, slightly displaced positions in the tetrahedron. We find δ=4.37±0.15 pm, B_{Si}=0.58 Å^2 and B_{Mg}=0.62 Å^2.

To summarize, we have used a large angle convergent beam electron diffraction technique to study the thermal vibrations of the atoms in Mg_2Si, and in particular the anharmonicity of the Mg atoms in their tetrahedral environment. With this technique, many reflections with large reciprocal vectors are at the Bragg position simultaneously. These reflections are highly sensitive to the thermal motion of the atoms, and in this study we determine with great accuracy the parameters describing the anharmonicity of the tetrahedral Mg atoms in Mg_2Si.

[1] J. M. Zuo, M. O'Keeffe, P. Rez, and J. C. H. Spence. *Phys. Rev. Lett.*, 78(25):4777–4780, Jun 1997.

[2] J. M. Zuo, M. Kim, M. O'Keeffe, and J. C. H. Spence. *NATURE*, 401(6748):49–52, SEP 2 1999.

[3] L. Wu, Y. Zhu, T. Vogt, H. Su, J. W. Davenport, and J. Tafto. *Phys. Rev. B*, 69(6):064501, Feb 2004.

[4] J. Tani and H. Kido. *Physica B-Condensed Matter*, 364(1-4):218–224, JUL 15 2005.

[5] V. K. Zaitsev, M. I. Fedorov, E. A. Gurieva, I. S. Eremin, P. P. Konstantinov, A. Yu. Samunin, and M. V. Vedernikov. *Physical Review B*, 74(4), JUL 2006.

[6] J. Tafto and T. H. Metzger. *Journal of Applied Crystallography*, 18(APR):110–113, 1985.

[7] D. Panke and E. Wolfel. *Zeitschrift fur Kristallographie Kristallgeometrie Kristallphysik Kristallchemie*, 129(1-4):9–&, 1969.

[8] B. Dawson, A. C. Hurlay, and V. W . Maslen. *Proceedings of the Royal Society of London Series A-Mathematical and Physical Sciences*, 298(1454):289–&, 1967.

[9] M. J. Cooper, K. D. Rouse, and B. T. M. Willis. *Acta Crystallographica Section A-Crystal Physics Diffraction Theoretical and General Crystallography*,

A 24(Part 5):484–&, 1968.

[10] M. J. Cooper and D. Panke. *Acta Crystallographica Section A-Crystal Physics Diffraction Theoretical and General Crystallography*, A 26:292–&, 1970.

[11] B. T. M. Willis. *Proceedings of the Royal Society of London Series A-Mathematical and Physical Sciences*, 274(1356):122+, 1963.

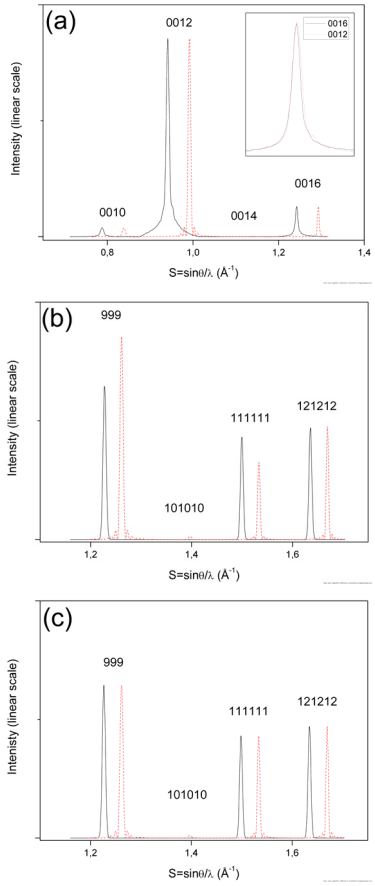

FIG. 3: Observed (solid line) and calculated (dotted line) intensity of the Bragg reflections. For the sake of comparison we have shifted the simulated profiles slightly to the right. (a) Linescan of the experiment and simulation along the 00h-row. The inset shows the scaled 0012 and 0016 reflections to indicate their similarly shaped backgrounds. In (b) and (c), a gaussian fit of the Bragg peaks of the hhh-row is used. (b) A simulation(dotted line) along the hhh-row without anharmonicity. (c) A simulation (dotted line) along the hhh-row with anharmonicity. The hkl indices are indicated above the reflections.

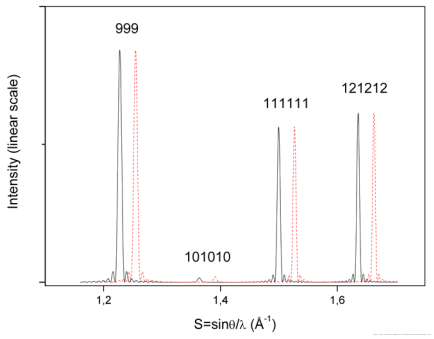

FIG. 4: Solid line is a simulation using the anharmonic parameter β. Dotted line is a simulation using the model suggested by Willis where the Mg atoms are displaced along the <111> direction of the unit cell. The hkl indices are indicated above the reflections.

Paper IV

K. Valset, P. H. M. Böttger, J. Taftøand T. Finstad
Thermoelectric properties of Cu doped p-type ZnSb containing Zn_3P_2 particles
To be submitted to Journal of Applied Physics

Thermoelectric properties of Cu doped ZnSb containing Zn_3P_2 particles

K. Valset,[1] P. H. M. Böttger,[1] J. Taftø,[1] and T. Finstad[1]

Department of Physics, University of Oslo, Blindern P.O. Box 1048, 0316 Oslo, Norway[a)]

We prepared ZnSb containing Zn_3P_2 particles of size ranging from a few tens to several hundred nanometers by melting powders of Zn, Sb and P. Materials with Zn_3P_2 content up to 3.75 % were made and subsequently ball-milled and hot pressed. A reduction in the thermal conductivity of 15 % was achieved. Doping with Cu increased the carrier concentration by an order of magnitude, to $2.0{\cdot}10^{19}\mathrm{cm}^{-3}$, while the mobility remained unaffected. The resulting increase in electrical conductivity together with the reduced thermal conductivity, led to a significant increase in the dimensionless figure of merit, in excess of 0.9 around 550 K.

[a)]Electronic mail: kjetil.valset@fys.uio.no

I. INTRODUCTION

The need for renewable energy has triggered extensive research in thermoelectric materials due to their ability to turn heat gradients into electrical energy. Thermoelectric modules are simple in construction and reliable, but if these materials are to be of significance for the general energy management their efficiencies have to be increased and the material costs have to go down. Zn-Sb alloys are considered to be promising with respect to these criteria. The efficiency is related to the thermoelectric figure of merit, zT=$\frac{\alpha^2\sigma}{\kappa_e+\kappa_l}$, where α is the Seebeck coefficient, σ the electrical conductivity, κ_l is the lattice thermal conductivity and κ_e is the electron thermal conductivity.

Zn-Sb alloys are found to have two stable binary phases at room temperature, ZnSb and β-Zn_4Sb_3. The $\beta - Zn_4Sb_3$ phase is found to have a higher zT than the ZnSb phase, to a large degree due to the low lattice thermal conductivity κ_l. This may be explained by its complex crystal structure, with interstitial zinc atoms distributed over multiple positions [1,2]. Previous reports from ball milled ZnSb found a room temperature κ_l of 2.26 W/mK, of a total thermal conductivity of 2.30 W/mK [3]. The phonon glass limit [4] for ZnSb was found to be 0.6 W/mK[5], suggesting a potential for improving zT through a reduction of κ_l.

There are several cases reported recently about reduction of the lattice thermal conductivity through introduction of nanoinclusions[6–8]. A reduction in κ_l is explained by scattering of the long wavelength phonons at the interfaces introduced by the nanoinclusions. Nanoinclusions can be introduced into bulk materials[9,10]. In this work we have formed nanoparticles of Zn_3P_2 inside a matrix of ZnSb to reduce κ_l. Substitution of antimony by phosphorus in ZnSb could also reduce κ_l. Short wavelength phonons may be scattered through the local distortion introduced by substitution atoms and by alloying a reduction in κ_l may be achieved[11].

The parameters α, σ and κ_e are dependent on the carrier concentration and can also be tuned to optimize $\frac{\alpha^2\sigma}{\kappa_e+\kappa_l}$ for a given κ_l [12]. To increase the carrier concentration in ZnSb/Zn_3P_2 mixed alloys we added Cu. Doping by Cu has been reported earlier for ZnSb[5] and Zn_3P_2[13]. By adding large amounts of Cu in Zn-Sb alloys, other Cu rich phases have also been reported[14].

II. EXPERIMENTAL DETAILS

The samples were prepared by melting the elements in evacuated silica glass ampoules. The purities were 99.99 % for Sb, Zn and 99.999 % for Cu, P. The material was quenched and grinded into powder and annealed at 505°C in vacuum for 3 days, followed by ball milling in an Argon atmosphere for 20 minutes in a stainless steel vial. The resulting powder was sintered by a uniaxial hot press, with a sintering pressure of 50 MPa. The temperature was kept close to the melting point to achieve high density samples. Samples of ZnSb with varying nominal content of Zn_3P_2 (0, 0.625, 1.5, 2.5, 3.75 at.%) were prepared. In addition, samples of ZnSb with 2.5 at.% Zn_3P_2 with varying nominal content of Cu (0.05, 0.1, 0.2 at.%) were prepared. All samples had a density above 6.05 g/cm^3, except for the sample made with 2.5 at.%Zn_3P_2 and 0.05 at.%Cu which had a density of 5.95 g/cm^3 (theoretical density of ZnSb is 6.4 g/cm^3). The Seebeck coefficient and the resistivity were measured in a custom built system[15] between RT and 340 °C. The Hall carrier concentration and mobility were measured by a Lake Shore Hall setup. The thermal conductivity was measured using a Netzsch Laser Flash (LFA 457). The samples were analyzed by X-ray diffraction (XRD), Transmission Electron Microscope (TEM) and Scanning Electron Microscope (SEM).

III. RESULTS AND DISCUSSION

A. ZnSb/Zn_3P_2 mixed alloys

When a melt of ZnSb containing small amounts of phosphorus was quenched, SEM analysis revealed phosphorus rich particles formed inside a matrix of ZnSb. By electron diffraction these particles were identified as α-Zn_3P_2, and samples of ZnSb were then prepared with varying nominal content of Zn_3P_2 between 0 and 3.75 at.%. The particles had sizes ranging from a few tens to several hundred nanometers (Fig. 1) and XRD spectra of these samples were found to be consistent with a single phase ZnSb for the matrix.

Our phase identification studies indicate that the solubility of P in ZnSb is low. It is relevant to discuss this in light of the bonding of ZnSb, the atomic sizes reported with that bonding and the phases known in phase diagrams. The dominating bonding in ZnSb is stated to be covalent[16] and X-ray photoelectron spectroscopy data confirms this[17]. The covalent radius for P and Sb is 1.07 and 1.39 respectively[18]. Dissolution of P in ZnSb will

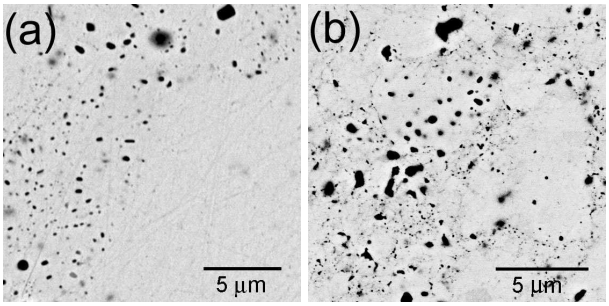

FIG. 1. SEM pictures taken in the backscattering mode from the preparation of ZnSb samples. White area is ZnSb while black areas are Zn_3P_2 particles. (a) ZnSb with 2.5 at.%Zn_3P_2 as solidified melt before grinding to powder. (b) ZnSb with 2.5 at.%Zn_3P_2 and 0.2 at. % Cu after grinding to powder and sintering.

TABLE I. Carrier concentration (p) and Hall mobility (μ_H) at room temperature for single phase ZnSb and ZnSb/Zn_3P_2 two phase mixtures.

Sample composition	p $[cm^{-3}]$	μ_H [cm^2/Vs]
0%Zn_3P_2	$1.4{\cdot}10^{18}$	177
0.625%Zn_3P_2	$5.5{\cdot}10^{17}$	238
1.5%Zn_3P_2	$7.0{\cdot}10^{17}$	214
2.5%Zn_3P_2	$8.9{\cdot}10^{17}$	179
3.75%Zn_3P_2	$5.3{\cdot}10^{17}$	252

thus cost energy, and since the Zn_3P_2 phase is more stable than the ZnSb phase, which can be inferred from their difference in melting temperature (>850 ^{o}C and 546 ^{o}C respectively) it is more favorable with the two phases than high concentrations of P in ZnSb. The low solubility of P in ZnSb can thus be qualitatively understood.

Figure 2 shows the results of the thermal conductivity measurements of ZnSb samples containing Zn_3P_2. As can be seen the thermal conductivity is between 0.15 $\frac{W}{mK}$ and 0.30 $\frac{W}{mK}$ lower for the mixed alloys than found for ZnSb (Fig. 2). A reduction in thermal conductivity can be expected as phonons may be scattered at the interface area introduced by the Zn_3P_2

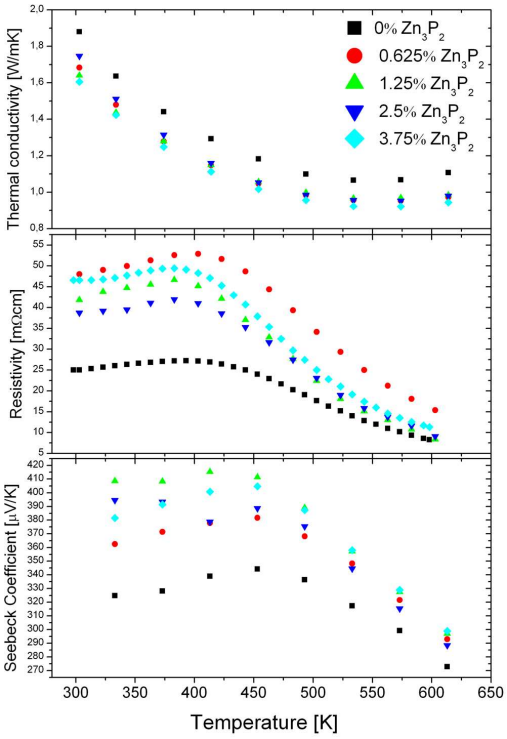

FIG. 2. Thermal conductivity, Electrical resistivity Seebeck coefficient for ZnSb containing Zn_3P_2.

particles. The uncertainties when measuring κ_l adds up to 7%, due to uncertainties in sample thickness, heat capacity and density. An increase in Seebeck coefficient and electrical resistivity is also found for the mixed alloys compared to ZnSb. Hall measurements (Table I) of the samples show a p-type conduction and the increase in electrical resistivity for the mixed alloys is due to a reduction in the carrier concentration. However, the Hall mobility is found to be higher for the mixed alloys.

B. Cu doped ZnSb/Zn_3P_2 mixed alloys

Samples of ZnSb/Zn_3P_2 mixed alloys were also made with 2.5 at.% Zn_3P_2 and between 0.05 at.% and 0.2 at.% copper to increase the carrier concentration. XRD θ-2θ measurements on these samples were also found to be consistent with a single phase ZnSb for the matrix.

TEM analysis of the ZnSb/Zn_3P_2 mixed alloys with 0.1 at.% Cu and 0.2 at.% Cu, reveals

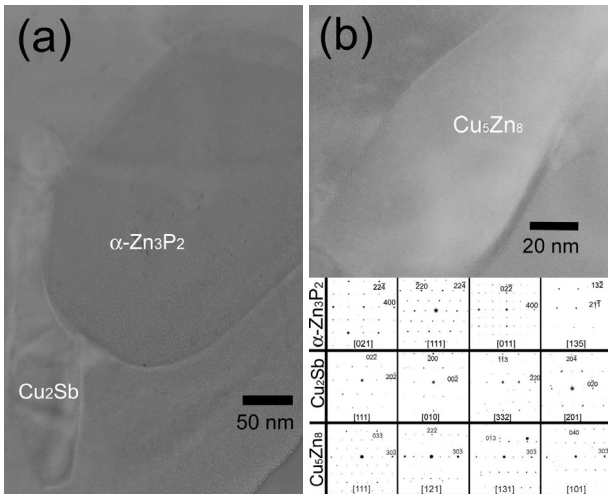

FIG. 3. (a) TEM picture of particle of Zn_3P_2 along with a Cu_2Sb particle. (b) Particle of Cu_5Zn_8. Diffraction pattern of Zn_3P_2, Cu_5Zn_8 and Cu_2Sb particles are shown at the bottom. The diffraction patterns of Cu_5Zn_8 and Cu_2Sb have additional diffraction spots from the surrounding matrix due to the small size of the particles.

Cu_2Sb and Cu_5Zn_8 particles in addition to Zn_3P_2 particles (Fig.3). Indication of a limit in the Cu solubility in ZnSb at concentrations above 0.1 at.% has been found earlier from the saturation of hole concentration with increasing Cu content[5]. For the sample with 0.2 at.% Cu the Cu_5Zn_8 particles were often stacked together. The Cu_2Sb particles were dispersed throughout the samples and were often found in vicinity of the Zn_3P_2 particles as seen in Fig.3 (a). The sizes of these particles were typically around 100 nanometers.

The room temperature electrical resistivity in the samples with 0.1 and 0.2 at.% Cu are an order of magnitude lower than the one found in ZnSb (Fig. 4). The carrier concentration found by Hall measurements at room temperature are presented in Table II and most of the decrease in resistivity can be explained by an increase in carrier concentration. The mobilities in the Cu doped mixed alloys are also higher than for the single phase ZnSb sample. The Cu_2Sb and Cu_5Zn_8 precipitates are expected to be of minor importance for the electrical conductivity in the mixed alloys as the Cu concentrations are very small, and as the trend in mobility is opposite of what has been observed earlier in Zn-Sb alloys containing the same Cu rich precipitates[14].

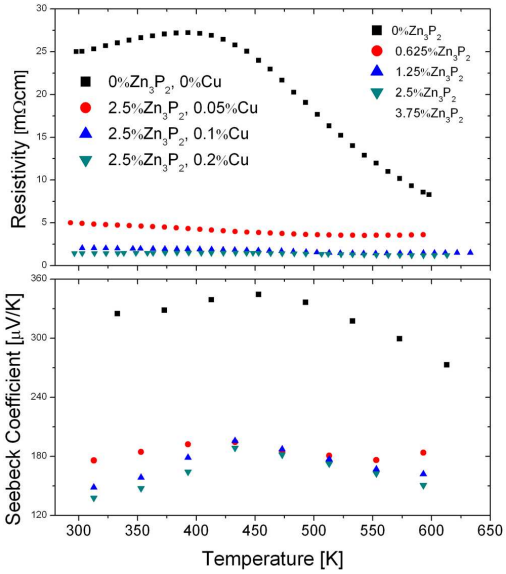

FIG. 4. Electrical resistivity Seebeck coefficient for ZnSb containing 2.5 at.% Zn_3P_2, doped with Cu. The Seebeck coefficient for the sample doped with 0.05 at.%Cu increases at temperatures above 600 K, and could be associated with a metallic/semiconductor transition in the Zn_3P_2 particles.

Zn_3P_2 is reported to be a semiconductor with a band gap of 1.55 eV[19]. It is usually p-type, which is believed to be due to excess P occupying tetrahedral interstitial sites. The thermoelectric properties of Zn_3P_2 doped with Cu (i.e. $Cu_xZn_{3-x}P_2$ ($0<x<0.08$)) has been reported[13]. The reported results indicates that Zn_3P_2 can be doped heavily by Cu; Nagamoto et al. reported metallic electric behavior below 600 K indicating degenerate doping. A sharp increase in resistivity and Seebeck coefficient was reported at temperatures above 600 K. This can tentatively be considered to be a characteristic of Zn_3P_2 doped to the solubility limit. If conduction in our ZnSb/Zn_3P_2 samples were influenced by the electrical properties of Zn_3P_2 particles, these strong changes could be expected to be present. A close examination of Fig. 4 reveal that there is a small increase in the Seebeck coefficient for the sample with 0.05 at.% Cu at around 600 K. However, no such significant increase in Seebeck coefficient was observed in the other copper doped samples above 600 K. Thus, we can not conclude that the small increase for the sample doped with 0.05 at.% Cu is directly connected to changes in properties of Zn_3P_2.

TABLE II. Carrier concentration (p) and Hall mobility (μ_H) at room temperature for single phase ZnSb and ZnSb/Zn_3P_2 mixed alloys doped with Cu. Effective mass (m*) is found from the Seebeck coefficient and carrier concentration using the single parabolic band model. Values are more uncertain in the sample with 0.05 at.% Cu due to a lower sample density.

Sample composition	p [cm^{-3}]	μ_H [cm^2/Vs]	m*
0%Zn_3P_2,0%Cu	1.4· 10^{18}	177	0.47
2.5%Zn_3P_2,0.05%Cu	5.8· 10^{18}	217	0.43
2.5%Zn_3P_2,0.10%Cu	1.8· 10^{19}	172	0.58
2.5%Zn_3P_2,0.20%Cu	2.0· 10^{19}	215	0.56

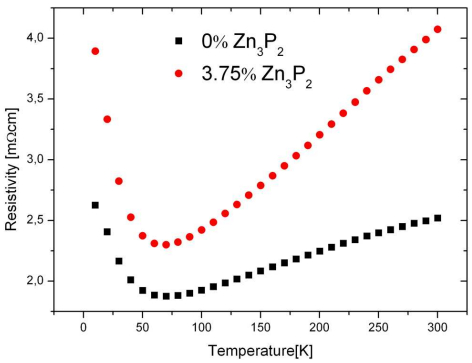

FIG. 5. Low temperature measurements of ZnSb and an alloy of ZnSb/Zn_3P_2 with 3.75 at.% Zn_3P_2.

An earlier study using Cu as dopant found that increasing the Cu content above 0.1 at.% did not result in a significant increase in the carrier concentrations[5]. We then achieved a maximum in carrier concentration of $8.0{\cdot}10^{18}$ cm^{-3}, while for ZnSb/Zn_3P_2 mixed alloys, the largest carrier concentration is found to be $2.0{\cdot}10^{19}$ cm^{-3} for the sample doped with 0.2 % Cu. The Hall mobilities in the mixed alloys are also found to be higher than for ZnSb, even if the carrier concentration is increased an order of magnitude. This is a peculiar observation that will be discussed further in the following.

At high carrier concentration a reduced mobility is usually observed due to impurity

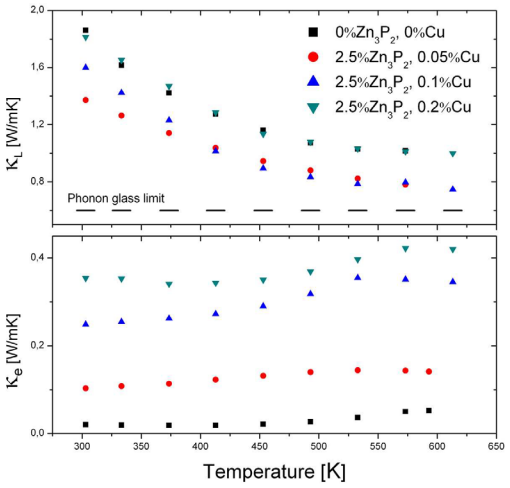

FIG. 6. Lattice thermal conductivity for ZnSb and ZnSb/Zn_3P_2 samples doped with Cu. The lattice thermal conductivity (κ_l) is calculated assuming a constant Lorenz number of $1.7{\cdot}10^{-8}\mathrm{W\Omega K^{-2}}$ for doped samples and $1.5{\cdot}10^{-8}\mathrm{W\Omega K^{-2}}$ for ZnSb. The dotted line is the phonon glass limit for ZnSb[5]

scattering. This also seems to be the general trend for ZnSb prepared in our lab for other investigations without Zn_3P_2 additions for carrier concentrations in the range $5{\cdot}10^{17}$ to $8{\cdot}10^{18}$ $\mathrm{cm^{-3}}$ at room temperature. The phonon scattering is dominating the temperature dependence of the mobility while the impurity scattering is significantly influencing the absolute value. The carrier mobility may be influenced by the presence of both compensating defect states as well as shallow acceptor centers. In such cases, the Hall mobility may be increased through doping as the ratio between compensating defects states and acceptor concentrations is altered[20].

Existence of compensating defect states in ZnSb introduced by phosphorus may be indicated by low temperature measurements. Low temperature measurements done on single phase ZnSb and ZnSb with 3.75 at.% Zn_3P_2 (Fig. 5) reveal a minimum in electrical resistivity due to impurity band conduction in addition to valence band conduction[5,21]. The minimum in resistivity is found at the same temperature regardless if Zn_3P_2 is added and the similarity between the curves suggests that the dominating acceptor level is the same. However, a compensating donor level can be nearly anywhere in the band gap and new

compensating levels may still have been introduced into the mixed alloys by phosphorus. The P addition could also remove existing compensating levels. These phenomena would alter the number of scattering centers.

Modulation doping is common for high mobility transistors in III-V heterojunctions. Modulation doping has also been suggested as a mean to increase zT[22]. The difference in band gap between Zn_3P_2 and ZnSb is in the region of 1 eV ($\sim$1.55 eV for Zn_3P_2[19] and 0.3-0.5 eV for ZnSb[3,23,24]) and as Cu doping may result in a metallic behavior in Zn_3P_2[13] indicating heavy doping effects, a large number of carriers may potentially diffuse to ZnSb. A high carrier concentration and mobility may then be achieved simultaneously as the free carriers in the matrix (ZnSb) are separated from the acceptor ions. For modulation doping by Zn_3P_2 to occur, there should be a positive valence energy band offset when going from Zn_3P_2 to ZnSb. The band alignment of ZnSb/Zn_3P_2 heterojunction is unknown, thus the likelihood of this mechanism for the present case can not be ascertained.

To derive κ_l we used the single parabolic band (SPB) approximation to calculated the Lorenz number from the Seebeck coefficient[25]. All samples containing Cu had a Seebeck coefficient between 138 V/K and 195 V/K yielding a Lorenz number around $1.7{\cdot}10^{-8}\mathrm{W\Omega K^{-2}}$. For ZnSb a Lorenz number of $1.5{\cdot}10^{-8}\mathrm{W\Omega K^{-2}}$ was used. It is seen that the lattice thermal conductivity never exceeds that of bulk ZnSb, however, a large increase in κ_l is found when the Cu doping is increased from 0.1 at.% to 0.2 at.% (Fig. 6). It is speculated that this can be explained by increased segregation at high Cu concentrations and the effective medium being more influenced by the precipitations the more abundant they are.

By Cu doping the ratio $\alpha^2\sigma/\kappa$ is increased resulting in a zT > 0.9 for the sample with 0.1 % Cu at temperatures around 550 K (fig. 7). Using the single parabolic band model, an optimized zT for ZnSb was expected to be achieved for carrier concentrations in the region of $2{\cdot}10^{19}$ $\mathrm{cm^{-3}}$ [5], suggesting that an optimized zT can be achieved through Cu doping of these mixed alloys. The value of the optimized carrier concentration will be dependent on the carrier mobilities and κ_l that may be achieved. The combined uncertainties ($\frac{\triangle zT}{zT}$) for these measurements (α, κ, σ) are considered to be 20%[26]. The Harman technique[27] was used to measure zT at room temperature (Table III) and found in close agreement with the results from the measurements of σ, κ and α in fig. 7.

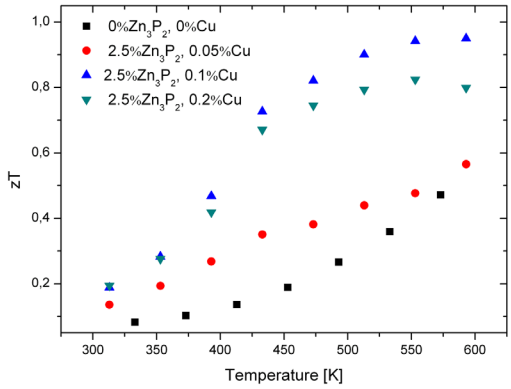

FIG. 7. Figure of merit(zT) for single phase ZnSb and Cu doped ZnSb containing 2.5 at.% Zn_3P_2.

TABLE III. Figure of merit at room temperature measured by the Harman technique

Sample composition	zT
2.5%Zn_3P_2, 0.05%Cu	0.13
2.5%Zn_3P_2, 0.10% Cu	0.18
2.5%Zn_3P_2, 0.20% Cu	0.18

IV. SUMMARY

Mixed alloys of ZnSb/Zn_3P_2 were found to have higher mobilities than those found in ZnSb. By doping with copper, the carrier concentrations in the mixed alloys were increased an order of magnitude compared to ZnSb, without reducing the mobilities. These copper doped mixed alloys are found to have higher carrier concentrations than what to our knowledge has been reported for single phase ZnSb earlier. This could be explained by an enhanced solubility of Cu in ZnSb by small additions of P, or due to modulation doping by Zn_3P_2. The optimum zT in Cu doped ZnSb/Zn_3P_2 mixed alloys was found to be close to unity at temperatures around 550 K.

REFERENCES

[1]G. J. Snyder, M. Christense, E. Nishibori, T. Caillat, and B. Brummerstedt Iversen, Nature Mater. **3**, 458 (2004).

[2]W. Schweika, R. P. Hermann, M. Prager, J. Persson, and V. Keppens, Phys. Rev. Lett. **99**, 12 (2007).

[3]L. T. Zhang, M. Tsutsui, K. Ito, and M. Yamaguchi, J. Alloys Compd. **358**, 252 (2003).

[4]David G. Cahill, S. K. Watson, and R. O. Pohl, Phys. Rev. B **46**, 6131 (1992).

[5]P. H. M Bttger, G. S. Pomrehn, G. J. Snyder, and T. Finstad, Phys. Status Solidi A, (2011) /it(In Print)

[6]N. Mingo, D. Hauser, N. P. Kobayashi, M. Plissonnier, and A. Shakouri, Nano Lett. **9**, 711 (2009).

[7]Chunlei Wan, Yifeng Wang, Ning Wang, Wataru Norimatsu, Michiko Kusunoki, and Kunihito Koumoto, Sci. Tech. Adv. Mater. **11**, 044306 (2010).

[8]Aleksei V Dmitriev and Igor P Zvyagin, Phys. Usp. **53**, 789 (2010).

[9]Joseph R. Sootsman, Robert J. Pcionek, Huijun Kong, Ctirad Uher, and Mercouri G. Kanatzidis, Chem. Mat. **18**, 4993 (2006).

[10]J. Androulakis, K.F. Hsu, R. Pcionek, H. Kong, C. Uher, J.J. D'Angelo, A. Downey, T. Hogan, and M.G.Kanatzidis, Adv. Mater. **18**, 1170 (2006).

[11]V. K. Zaitsev, M. I. Fedorov, E. A. Gurieva, I. S. Eremin, P. P. Konstantinov, A. Yu. Samunin, and M. V. Vedernikov, Phys. Rev. B **74**, 045207 (2006).

[12]G. Jeffrey Snyder and Eric S. Toberer, Nature Mater. **7**, 105 (2008).

[13]Y Nagamoto, K Hino, H Yoshitake, and T Koyanagi, Proc.1XVII Int. Conf. Thermoelectrics (ICT 98), 24-28 May 1998, Nagoya, Japan, p 354

[14]J.L. Cui, L.D. Mao, D.Y. Chen, X. Qian, X.L. Liu, and W. Yang, Curr. Appl. Phys. **9**, 713 (2009).

[15]P. H. M. Böttger, PhD thesis University Of Oslo, (2011).

[16]Arkady S. Mikhaylushkin, Johanna Nylen, and Ulrich Haussermann, Chem.Eur. J. **11**, 4912 (2005).

[17]P. H. Michael Böttger, Spyros Diplas, Espen Flage-Larsen, Oystein Prytz, and Terje G Finstad, J. Phys.: Condens. Matter **23**, 265502 (2011).

[18]Beatriz Cordero, Veronica Gomez, Ana E. Platero-Prats, Marc Reves, Jorge Echeverria, Eduard Cremades, Flavia Barragan, and Santiago Alvarez, Dalton Trans. **21**, 2832 (2008).

[19]A. M. Hermann, Arun Madan, M. W. Wanlass, V. Badri, R. Ahrenkiel, Scott Morrison, and Carlos Gonzalez, Sol. Energy Mater. Sol. Cells **82**, 241 (2004).

[20]In-Hwan Lee, In-Hoon Choi, Cheul-Ro Lee, Sung-Jin Son, Jae-Young Leem, and Sam Kyu Noh, J. Cryst. Growth **182**, 314 (1997).

[21]E. Justi, W. Rasch, and G. Schneider, Adv. Energ. Conv. **4**, 27 (1964).

[22]Mona Zebarjadi, Giri Joshi, Gaohua Zhu, Bo Yu, Austin Minnich, Yucheng Lan, Xiaowei Wang, Mildred Dresselhaus, Zhifeng Ren, and Gang Chen, Nano Lett. **11**, 2225 (2011).

[23]P. J. Shaver and John Blair, Phys. Rev. **141**, 649 (1966).

[24]N. F. Mott, Adv. in Phys. **50**, 865 (2001).

[25]H. J. Goldsmid, Applications of Thermoelectricity (Methuen, London, 1960).

[26]Kuei Fang Hsu, Sim Loo, Fu Guo, Wei Chen, Jeffrey S. Dyck, Ctirad Uher, Tim Hogan, E. K. Polychroniadis, and Mercouri G. Kanatzidis, Science **303**, 818 (2004).

[27]T. C. Harman, J. Appl. Phys. **29**, 1373 (1958).